

Reaction Enthalpies of Metal-Polyimide Interface
Formation Observed by Calorimetry

by

Richard Murdey

B.Sc., Memorial University of Newfoundland, 1995

A THESIS SUBMITTED IN PARTIAL FULFILMENT OF
THE REQUIREMENTS FOR THE DEGREE OF

DOCTOR OF PHILOSOPHY

in

THE FACULTY OF GRADUATE STUDIES

(Department of Chemistry)

We accept this thesis as conforming
to the required standard

~
THE UNIVERSITY OF BRITISH COLUMBIA

July 6, 2003

© Richard Murdey, 2003

In presenting this thesis in partial fulfilment of the requirements for an advanced degree at the University of British Columbia, I agree that the Library shall make it freely available for reference and study. I further agree that permission for extensive copying of this thesis for scholarly purposes may be granted by the head of my department or by his or her representatives. It is understood that copying or publication of this thesis for financial gain shall not be allowed without my written permission.

Department of Chemistry

The University Of British Columbia
Vancouver, Canada

Date July 7th 2003

Abstract

A calorimeter has been developed to study metal-polymer interfaces in ultra-high vacuum (UHV) conditions. Metal atoms are pulsewise deposited on a polymer substrate, gradually forming a metallic overlayer, while the reaction heat is measured in-situ with a pyroelectric sensor. Differential enthalpies of interface formation are derived from the calorimetry data and reported as a function of metal coverage. The ability of the instrument to resolve the underlying chemical reactions and growth morphology that characterize these interfacial systems is confirmed by the widely different enthalpy curves observed for each of the three metals studied in the present work - calcium, chromium and copper - deposited on PMDA-ODA polyimide substrates and the correspondingly distinct conclusions about the interfacial reactivity that were made in each case: Strong binding was discovered at the interface between calcium and polyimide. A calcium-polyimide complex with a binding energy of 600 ± 20 kJ/mol is suggested from the high initial intensity and exponential decay of the observed enthalpies with increasing metal coverage. The surface density of calcium binding sites was estimated at 4.1 nm^{-2} . A more complicated reactivity was observed for the chromium-polyimide interface. Reaction enthalpies of approximately 60 ± 20 kJ/mol were observed at low coverages, six times lower than the enthalpy of formation of bulk chromium metal. This indicates the creation of a thermodynamically

unstable interface. Chromium deposition apparently induces an endothermic disruption of the polyimide surface, which both lowers the net reaction enthalpy and suppresses the formation of metal-metal bonds. The copper results, meanwhile, are consistent with the formation of spherical metal clusters. The calorimeter records the change in surface energy from which the physical properties of the metal clusters, such as the cluster size, can be determined as a function of coverage.

Contents

Abstract	ii
Contents	iv
List of Tables	vii
List of Figures	viii
Acknowledgements	x
Introduction	1
1 Apparatus	4
1.1 Calorimeter System Overview	4
1.2 The Pyroelectric Heat Sensor	8
1.2.1 Pyroelectric Materials and Selection Criteria	8
1.2.2 Fundamental Equations	9
1.2.3 Calculation of the Voltage Response	12
1.2.4 Amplification and Signal Conditioning	18
1.2.5 Calibration	22
1.3 The Metal Atom Beam	24
1.3.1 The Evaporation Source	24
1.3.2 The Beam Chopper	25

1.3.3	The Velocity Selector	25
1.3.4	Stability of the Metal Atom Beam Flux	43
1.4	Sample Management	43
1.5	The Ultrahigh Vacuum Environment	44
1.6	Vibration Control and Noise	48
2	Experimental	50
2.1	Preparation of the Polymer Substrates	50
2.2	Preparation of the Metal Atom Beam	51
2.3	Procedures for Running a Calorimetry Experiment	52
2.4	Treatment of Raw Data	53
2.4.1	Pulse Height Measurement	53
2.4.2	Subtraction of the Optical Baseline	54
2.4.3	Conversion to the Calorimetric Molar Heat	55
2.4.4	Conversion of the Measured Enthalpy to Standard Con- ditions	56
2.4.5	Conversion from Differential to Integral Enthalpy	57
3	Results	58
3.1	Calcium, Copper and Chromium Deposition on Polyimide	58
3.1.1	Calcium on Polyimide	59
3.1.2	Chromium on Polyimide	62
3.1.3	Copper on Polyimide	65
3.2	Reproducibility of the Calorimetry Data	68
3.3	Comments on the Optical Baseline	68

4 Discussion	71
4.1 PMDA-ODA Polyimide Films	71
4.2 Calcium on Polyimide	72
4.2.1 Literature Review	72
4.2.2 Analysis of the Calorimetry Data	74
4.3 Chromium on Polyimide	78
4.3.1 Literature Review	78
4.3.2 Analysis of the Calorimetry Data	80
4.4 Copper on Polyimide	83
4.4.1 Literature Review	83
4.4.2 Binding Energy of Model Copper Clusters	84
4.4.3 Analysis of the Calorimetry Data	86
Conclusion	90
Bibliography	94

List of Tables

1.1	Material Properties of Lithium Tantalate	9
1.2	The Electrical and Thermal Properties of the Pyroelectric De- tector	18
1.3	Calculated Kinetic Energy of the Metal Atom Beam for Se- lected Experimental Conditions	36
1.4	Relevant Dimensions and Operational Specifications of the Ve- locity Selector	37
1.5	Noise Measurements of the Calorimeter Output Signal Under Various Operating Conditions	48
3.1	Metal Deposition Conditions and Related Experimental Pa- rameters	58
4.1	Electrochemical Potentials of PMDA-ODA Polyimide and Se- lected Metals	74

List of Figures

1.1	Schematic Illustration of the Calorimeter	7
1.2	Response of the Pyroelectric Sensor to a Step Input	13
1.3	Simulated Response of the Pyroelectric Detector to a Square Pulse	17
1.4	jFET Preamplifier Circuit Schematic	19
1.5	Voltage Amplifier Circuit Schematic	21
1.6	Calorimeter Linearity	23
1.7	Schematic Illustration of the Evaporation Source and Beam Chopper	26
1.8	An Illustrative Sketch of a Slotted Disc Velocity Selector . . .	28
1.9	An Illustrative Sketch of a Slotted Disc Velocity Selector, with Modifications for a Non-perpendicular Particle Trajectory . . .	31
1.10	Transmission and Velocity Distribution Functions for the Ve- locity Selector	35
1.11	Schematic Illustration of the Velocity Selector	39
1.12	Calculated Flux Gradient Across the Sample Width	41
1.13	Transmission of the Velocity Selector as a Function of Blade Speed	42
1.14	The Modified ESCA Mk. I Sample Mount	45
1.15	Residual Gas Analysis of the Calorimetry UHV Chamber . . .	47

2.1	Condensation Reaction of Polyamic Acid	51
3.1	Calorimeter Response for Calcium Deposition on Polyimide. .	60
3.2	Differential Reaction Enthalpy of Calcium-Polyimide Interface Formation	61
3.3	Calorimeter Response for Chromium Deposition on Polyimide.	63
3.4	Differential Reaction Enthalpy of Chromium-Polyimide Inter- face Formation	64
3.5	Calorimeter Response for Copper Deposition on Polyimide. . .	66
3.6	Differential Reaction Enthalpy of Copper-Polyimide Interface Formation	67
3.7	Differential Reaction Enthalpy of Chromium-Polyimide Inter- face Formation, Variance Between Trials	69
4.1	Chemical Structure of PMDA-ODA Polyimide	72
4.2	Exponential Fit of the Adsorption Enthalpy of Calcium De- posited on Polyimide	76
4.3	Differential Reaction Enthalpy of Chromium-Polyimide Inter- face Formation	81
4.4	Copper Cluster Densities Derived from Calorimetry and XPS Data	87
4.5	Calculated Binding Energies for Spherical Copper Clusters . .	89

Acknowledgements

I wish to thank my supervisor, Dr. J. T. Stuckless, for his patience, support and timely suggestions.

Thanks are also extended to Dr. M. Thachuk, Dr. D. Bizzotto and Dr. Jan Richter for helpful discussions.

I would like to acknowledge the expertise of the technical staff in the construction of the apparatus, especially Mr. Ken Love and Mr. Cedric Neale who between them did most of the in-house machining and fabrication.

I am indebted to the members of the Metal/Molecule Interfaces group who contributed to the project: Mr. Youngku Sohn, Mr. John Kim, Mr. Sam Liang, and Mr. Sherman Hon. I am grateful also for their many gestures of friendship and encouragement.

Financial support was provided by the National Science and Engineering Research Council.

Introduction

Interfacial reactions or morphological changes at metal-polymer interfaces have been previously studied by X-ray photoelectron spectroscopy (XPS), near edge X-ray fine structure absorption spectroscopy (NEXAFS), ultraviolet photoelectron spectroscopy (UPS), and other spectroscopic and imaging techniques. [1–5] Predictions about the strength of chemical bonds at the interface are frequently made from data obtained by theoretical and spectroscopic [6–8] as well as imaging [9] studies, yet neither the enthalpy of interface formation nor experimentally derived metal-polymer binding energies have been published. A direct measurement of these properties, as provided by calorimetry, would both verify existing predictions and, it is anticipated, generate new information about the metal-polymer interface.

Calorimetry as a modern surface science technique was pioneered by D. A. King et al. at Cambridge in the late 1980's to study the reactions of light molecules like oxygen or carbon monoxide on single-crystal metal surfaces. [10, 11] The measurement of the heat of adsorption on small surfaces has a rich history going back much further, for a comprehensive review see Černý [12]. Apart from the improved vacuum, the use of a molecular beam to deliver the adsorbate distinguished the Cambridge instrument from those that came before it. High adsorbate fluxes were now possible under ultrahigh vacuum (UHV) conditions, focused cleanly on a defined surface

area. The thermal detector, an external infrared sensor, was also significantly more sensitive than the thermocouples and resistive elements used earlier. The sensitivity was reliant upon the samples having very low heat capacity, in practice they had to be made extremely thin. [11] A similar instrument for poly-crystalline samples employing a pyroelectric heat sensor made from lithium tantalate (LiTaO_3) was built by Kovar et al. [13] while the heat of adsorption of metal atoms on metal oxide substrates was observed by C. T. Campbell's group at the University of Washington. [14] The detection element in the latter experiment was a thin polyvinylidene fluoride (PVDF) pyroelectric film.

In this work surface calorimetry techniques are further developed to investigate technologically relevant metal-polymer interfaces. Low dielectric insulating polymers are widely used in packaging applications such as at the interconnect level in multichip modules. [15] The interface between the polymer and the conducting metal interconnects must be chemically and thermally stable, with little or no inter-diffusion. The development of semi-conducting polymers has dramatically broadened the scope of polymers in microelectronics applications, with a renewed interest in the properties of metal-polymer and polymer-polymer interfaces. [16–18] Interfacial properties such as adhesion, thermal stability, or charge injection significantly affect device performance. Metal-semiconducting polymers are commonly found in organic light emitting devices (OLEDs), field effect transistors (FETs) and solar cells. [19–22] Polymer-based integrated circuits are being developed. [23] In many of these systems

A calorimeter specifically designed to measure the reaction enthalpy of

metal atoms deposited on polymer substrates was constructed. The metal atoms were deposited by thermal evaporation and the polymer substrates by spin coating, both processes being commonly used in the fabrication of real devices. The UHV chamber and atom beam line were purpose-built, as was the calorimeter detector, electronics, and sample transfer system. The instrument is described in detail in Chapter 1.

The experimental procedure is set out in Chapter 2. The polymer sample, a thin film one centimeter in diameter, was spin-coated on a lithium tantalate crystal. Metal atoms from a pulsed beam condensed at the sample surface. The heat energy produced in the ensuing reaction diffused into the pyroelectric detector, generating a voltage peak. The molar enthalpy of reaction was derived as a function of metal coverage from the magnitude of the observed peak height. The experiment was performed under UHV conditions which together with a small sample surface area and standard sample mount ensures broad compatibility with existing surface science techniques for metal-polymer interface characterization.

Results are presented in Chapter 3 for the deposition of calcium, copper, and chromium atoms on pyromellitic dianhydride oxydianiline (PMDA-ODA) polyimide substrates. A low dielectric insulator, polyimides have good thermal and chemical stability and are widely used in microelectronics packaging applications. [15, 24, 25] Metal-polyimide interfaces have been subject to numerous studies since the early 1980's. The interpretation of the calorimetry results is discussed in Chapter 4 in the context of this available literature. A picture of the interfacial reactivity and growth is developed for each metal.

Apparatus

The calorimeter was constructed to measure the reaction heats of metal atoms deposited on polymer surfaces under UHV conditions. After an overview of the apparatus, the heat sensor and the associated electronics are treated in detail. The simulated response of the detector is derived from fundamental equations, and calibration procedures are described. Next the metal atom beam is examined. Finally the sample transfer system is illustrated.

1.1 Calorimeter System Overview

The apparatus is conceptually divided into four parts:

1. The calorimeter, by which is meant the device that measures the reaction heat. This includes the pyroelectric heat sensor and associated electronics.
2. The metal atom beam line, including the thermal evaporation source that generates the metal atom vapor, the beam chopper, velocity selector, and collimation apertures. Beam intensity was monitored by a quartz crystal microbalance.
3. The sample, including preparation and transfer. Polymer films were prepared by spin coating. The final curing/degassing was done under UHV.

4. The UHV chamber, and other ancillary equipment required to provide and maintain the vacuum, measure the pressure and residual gases, and isolate the apparatus from external sources of vibration.

The general layout of the apparatus is shown in Figure 1.1. A gate valve divides the stainless steel UHV chamber into two sections: the main calorimetry chamber containing the metal atom beam and heat sensor, and a smaller sample preparation chamber. UHV can be maintained in the main chamber while the preparation chamber is brought to atmosphere to add or remove a sample through a quick-access port. A linear transfer rod is used to transfer the sample from one chamber to the other.

The evaporation source, a resistively heated crucible (High Temperature Effusion Cell from Applied EPI) is located in the bottom section of the main chamber, surrounded by a stainless steel water cooling jacket. This section is differentially pumped and opens on the main chamber through a 4×25 mm aperture.

Directly above the effusion source is the beam chopper, a rotating disc with a single notch which generates the pulsed metal atom beam. The velocity selector is positioned between the beam chopper and the polymer sample. It attenuates optical radiation generated by the hot evaporation source that would otherwise saturate the detector. Modulation of the atom beam flux by the velocity selector occurs at sufficiently high frequency that it is time averaged by the calorimeter detector and can be neglected.

The quartz crystal microbalance (Inficon XTM/2 with standard sensor) is swung into position in front of the polymer sample to monitor the intensity and stability of the metal atom beam. It also serves as an effective beam

stop.

A mass spectrometer is available to check the composition of the residual gases found in the vacuum chamber.

The polymer sample is applied by spin coating to the surface of a pyroelectric heat sensing element (A LiTaO_3 disc from Deltronic Crystal Industries) that is then placed in a copper sample stub loosely based on the ESCA Mk. I sample mount commercially available for surface science analysis. The sample stub is moved between the calorimeter and sample heater using manipulators - "wobble sticks" - and translation stages. When attached to the calorimeter detector, the heat sensing element inside the sample stub connects to external electric circuitry that buffers and amplifies the signal.

A computer data acquisition and control card (National Instruments AT-MIO-16XE-50) operated under the LabView programming environment handles the acquisition of the pyroelectric signal and controls both the beam chopper and velocity selector.

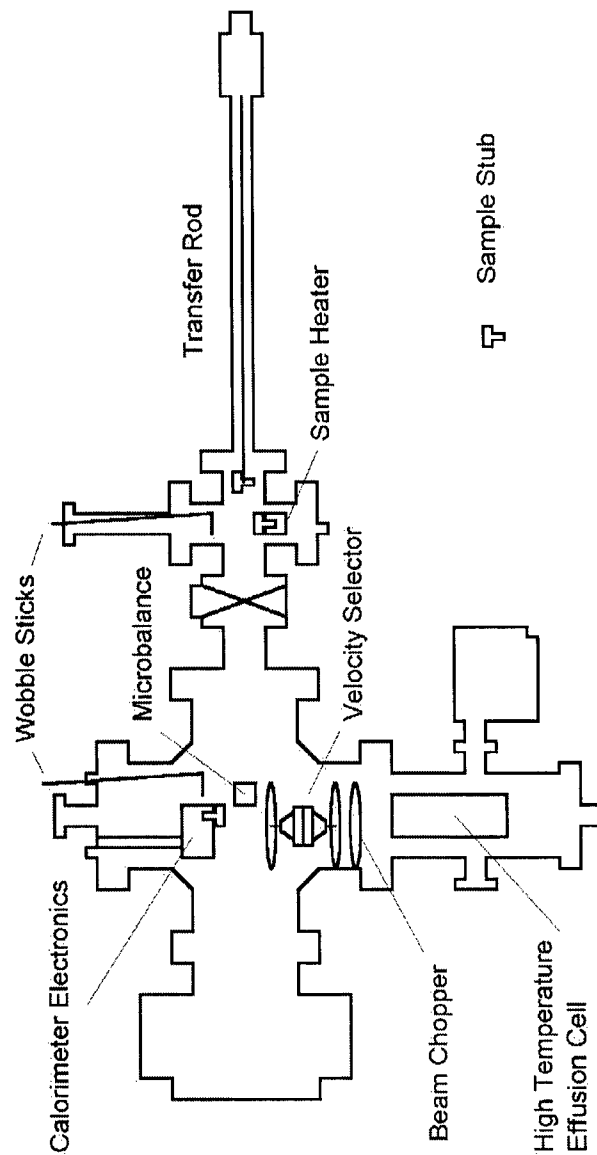


Figure 1.1: Schematic illustration of the surface adsorption calorimeter, showing the general layout of the UHV chamber and the position of key components located inside it. It was specifically designed for the study of polymer metallization.

1.2 The Pyroelectric Heat Sensor

The calorimeter detector employs a lithium tantalate pyroelectric sensor to measure the heat of the metal deposition reaction. The sensor is operated in voltage mode, and in this section the supporting electronics are described in detail. Calibration is also discussed. First, however, pyroelectric materials are introduced, followed by a mathematical derivation of the detector response.

A general introduction to thermal sensors can be found in “Fundamentals of Infrared Detector Operation and Testing” by J. D. Vincent. [26] The operation and theory of pyroelectric detectors is reviewed in the articles by Porter [27] and Whatmore [28].

1.2.1 Pyroelectric Materials and Selection Criteria

A pyroelectric material has an inherent electrical polarization, the magnitude of which changes with temperature. The surface charge will adjust to balance the polarization, and this charge when made to flow through an external circuit generates a signal voltage. A pyroelectric sensor is not a thermometer. Instead, either the amount or the rate of flow of the heat energy that enters the material is measured. The ability to measure the amount of heat makes it useful for calorimetry. UHV surface adsorption calorimeters have been built using two of these materials, polyvinylidene difluoride (PVDF) [14, 29, 30] and lithium tantalate [13].

The choice of material depends on the experimental requirements. Other properties than sensitivity are usually decisive, these include cost, available size, as well as mechanical, chemical and thermal stability.

Table 1.1: The material properties of lithium tantalate required to estimate the magnitude of the pyroelectric response. Values given at 25°C where relevant.

	Value	Unit	Reference
Pyroelectric Coefficient, p	2.3×10^{-4}	C/m ² /K	[28]
Curie Temperature, T_c	620	°C	[27]
Volume Specific Heat, s	3×10^6	J/m ³ /K	[27]
Resistivity, ρ	10^{13}	$\Omega \cdot \text{m}$	[27]
Dielectric Constant, ϵ	47		[28]

The requirement that the detector withstand the 400 °C cure cycle used to cure polyimide films dictated the use of lithium tantalate for the present study. Lithium tantalate, LiTaO₃, a ferroelectric material, maintains an electrical polarization until its Curie temperature, 620 °C. This is an exceptionally high value. [27] Fortunately it is also a very good pyroelectric, rugged, and readily available in the appropriate crystal dimensions. Lithium tantalate is commonly used as the active device in laser power meters and a wide range of commercial infrared sensors. Single-crystal discs were purchased from Deltronic Crystal Industries. They were gold plated on both faces with an interlayer of chromium for improved adhesion. The electrodes collect surface charge and facilitate its injection into the external circuit. The crystal diameter was 10.7 mm and the thickness approximately 0.5 mm. The material properties of lithium tantalate are presented in Table 1.1.

1.2.2 Fundamental Equations

In this section the mathematical relationship between the voltage response of the pyroelectric detector and the heat input is presented. A heat flux

causes the temperature of the pyroelectric material to change and a charge proportional to the temperature differential to be generated. When this charge flows through an electrical resistance the signal voltage is generated. The mathematical development follows the outline given in Chirtoc et al. [31], which highlights the symmetry of the two pertinent thermal and electrical differential equations. The thermal equation that equates the heat input to the rate of change of temperature of the detector has the same form as the electrical equation that equates the current generated to a signal voltage. The pyroelectric coefficient, p , links the two equations by equating the differential of the temperature to the differential of the charge, commonly known as the electrical current.

The electrical differential equation has as parameters the resistance, R , capacitance, C , and the product of the two which is called the electrical time constant, τ_E . The equivalence of the two equations means the parameters of the thermal differential equation can be specified in the same way: thermal resistance, R_T , thermal capacitance, C_T , - commonly known as the heat capacity - and a thermal time constant, τ_T , equal to $R_T \times C_T$.

The time constants may be regarded as a measure of the "speed" of the system. Smaller time constants result in faster response. In the thermal system, the temperature changes more quickly to a given heat signal. In the electrical system, the voltage responds more quickly to a given current.

The thermal differential equation is derived from the principle of conservation of energy. The pyroelectric is taken to be in contact with an infinite heat sink. The difference in temperature between the pyroelectric and heat sink is θ . The rate of change of θ depends on the rates of heat delivery

given as W and the rate of heat extraction to the heat sink which is proportional to θ itself. Heat extraction is regulated by the thermal conductance, R_T , while both terms are divided through by the heat capacity to give the desired temperature differential.

$$\frac{d\theta(t)}{dt} + \frac{\theta(t)}{\tau_T} = \frac{1}{C_T} W(t) \quad . \quad (1.1)$$

The temperature differential results in a charge differential in the pyroelectric material appearing along opposite ends of the axis of polarization. When the two ends are connected through an external circuit current will flow. The current, I , is a function of the pyroelectric coefficient, p , and the electrode area, A ,

$$I(t) = pA \frac{d\theta(t)}{dt} \quad . \quad (1.2)$$

The external circuitry can either measure the current directly (current mode operation) or the voltage generated as the current flows through a resistance, R , placed across the electrodes (voltage mode operation). At the low frequencies encountered in the calorimetry experiments, voltage mode operation is preferred. [32] When operated in voltage mode the voltage $V(t)$ across R is given by the charge transfer equation,

$$\frac{dV(t)}{dt} + \frac{V(t)}{\tau_E} = \frac{1}{C} I(t) \quad . \quad (1.3)$$

As noted above, Equation 1.3 is analogous to Equation 1.1. R is technically the parallel resistance of the load resistor and the pyroelectric sensor, while C is the total capacitance of the circuit,

$$\begin{aligned} R &= \left(\frac{1}{R_{load}} + \frac{1}{R_{element}} \right)^{-1} \\ C &= C_{element} + C_{input} + C_{stray} \quad , \end{aligned}$$

but for all the configurations encountered in this work, the assumptions that $R \approx R_{load}$ and $C \approx C_{element}$ remain valid.

1.2.3 Calculation of the Voltage Response

First, the case where the heat input is a step function is considered. The step function, $\Phi(t - t_0)$, is examined for $t_0 = 0$ such that the heat pulse begins at time zero. The incident power is given by $W(t) = W_o\Phi(t)$. The three equations given in Section 1.2.2 can be solved as follows for the voltage time response $V(t)$ given $V = 0$:

$$V(t) = \frac{W_o p A R_T R}{\tau_T - \tau_E} \left(e^{\frac{-t}{\tau_T}} - e^{\frac{-t}{\tau_E}} \right)$$

or

$$V(t) \propto \left(e^{\frac{-t}{\tau_T}} - e^{\frac{-t}{\tau_E}} \right) \quad (1.4)$$

It is observed that the pulse shape is defined by the two time constants. Fitting Equation 1.4 to the measured response of the detector to a step input is a convenient way to determine both time constants simultaneously. As the time constants are interchangeable due to the symmetry of the thermal and electrical differential equations in Section 1.2.2 it isn't possible to assign τ_T and τ_E unequivocally without further information. This assignment can be made by either repeating the measurement with a different value of R , or if the crystal capacitance is known, using the calculated electrical time constant as a guide. The results of this simple calibration are shown in Figure 1.2. The thermal time constant is 485 ms, and the electrical time constant is 60 ms.

Next the voltage response to a square pulse is determined, simulating the response of the detector to the pulsed atom beam used in the calorimetry

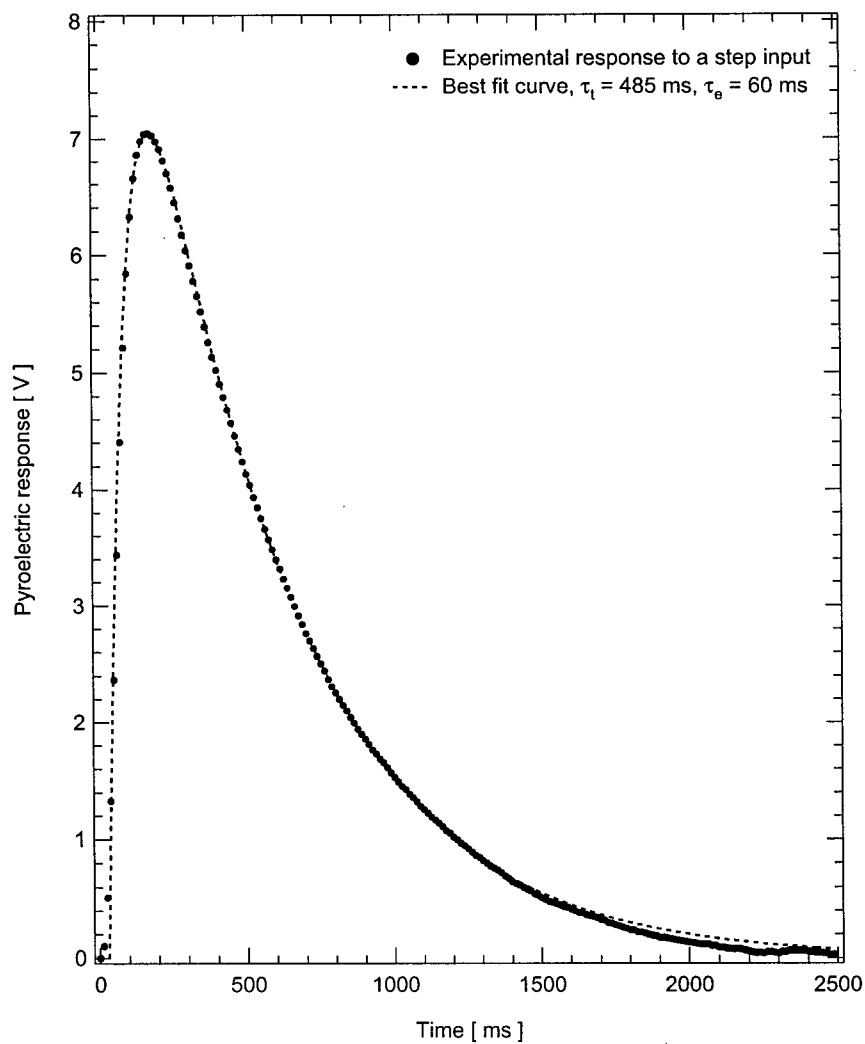


Figure 1.2: The response of the pyroelectric detector to turning on an incandescent light bulb outside the vacuum chamber. This data was used to determine the thermal and electrical time constants of the detector. The simulated response is also shown, scaled to the experimental data.

experiments. The pulse is defined as having a repeat length, t_{max} and an on time, t_{on} . The duty cycle is t_{on}/t_{max} , and the off time $t_{max} - t_{on}$. The heat input signal becomes $W(t) = W_o[\Phi(t - t_0) - \Phi(t - t_0 - t_{on})]$.

When $0 \leq t \leq t_{on}$ the voltage response is

$$V_{on}(t) = \frac{W_o p A R_T R}{\tau_T - \tau_E} \left(e^{\frac{-t}{\tau_T}} - e^{\frac{-t}{\tau_E}} \right) \quad . \quad (1.5)$$

When $t_{on} \leq t \leq t_{max}$ the input power W_o is zero and the voltage decays according to the following expression:

$$V_{off}(t) = V_{on}(t) - V_{on}(t - t_{on}) \quad . \quad (1.6)$$

Using these equations, it is possible to determine how best to adjust the pulse parameters and other available variables to optimize the detector for the calorimetry experiment, where the heat is produced by atoms deposited with a similar pulse profile. For a fixed input power W_o it would be easy to maximize the height of the voltage peak were it not for various limiting factors, namely,

1. The amount of energy delivered within one thermal time constant should not significantly raise the temperature of the detector.
2. To avoid the signal from one pulse overlapping with the next, the voltage output should decay to nearly zero during the off cycle.
3. An increase in signal obtained by changing the pulse rate may be more than offset by a change in the background noise.

Of the four variables that make up the electrical and thermal time constants, R , R_T , C , and C_T , only the resistance, R , is external and freely

variable. (Within the constraint that $R_{load} \ll R_{element}$, so that $R \sim R_{load}$.) The rest are fixed by the geometry of the pyroelectric sensor. The pulse parameters t_{max} and t_{on} are in practice defined by the beam chopper's rotational speed and duty cycle. They are variable within mechanical limits.

As the voltage response is largely controlled by the smaller of the two time constants, reducing R to ensure that the electrical time constant dominates results in the most flexible system. Given point 3, above, there will always be some trial and error involved, so such flexibility is very helpful in fine tuning the detector for the best signal-to-noise ratio.

As for the decay of the signal between pulses, point 2, it is noted that after five time constants have elapsed an exponential decay has less than 1% of the original magnitude. This is sufficiently close to zero for the purposes of the experiment, setting the condition that

$$t_{off} = 5 \tau_E \quad . \quad (1.7)$$

To maximize the signal, both t_{on} and τ_E should be as large as possible. This means $t_{on} = \tau_E$, and by application of Equation 1.7,

$$t_{max} = 6 t_{on} = 6 \tau_E \quad , \quad (1.8)$$

setting the duty factor of the pulse at 16.6%. The only remaining relation is between τ_T and τ_E . As explained above, τ_E should be less than τ_T , but the higher the value, the greater the voltage signal. The tradeoff is between signal ($\tau_E = \tau_T$) and flexibility ($\tau_E \ll \tau_T$), a decision which depends on the relative importance of the two. Keeping the electrical time constant about six times less than the thermal time constant was found to be a good compromise, and

was an easy rule-of-thumb to remember, since $\tau_T = t_{max}$ and the pulse rate, $1/t_{max}$, can then be set from the observed thermal time constant.

The time constants of the lithium tantalate sensor were found by observing the response to a step input, as described in Section 1.2.3. The thermal time constant was 485 ms. From the discussion above, the heat input pulse should have a duty factor of 16.6%, and repetition rate of $1/\tau_T = 2$ Hz. The electrical time constant should be approximately $\tau_T/6 = 80$ ms.

In practice, the nearest available load resistance was 500 M Ω , fixing the electrical time constant at 60 ms. The pulse repetition rate was 3.9 Hz and the duty cycle 16.6%. These parameters are all close to the optimal calculated values. With these pulse parameters combined with the properties listed in Table 1.2 the complete voltage pulse was simulated for various values of R using Equations 1.5 and 1.6. The results, shown in Figure 1.3, show the tradeoff between the signal height and decay time. It can be seen that some of the curves decay to below zero. This is the contribution of crystal cooling, which generates a voltage component of the opposite sign to the heat signal.

The preceding derivation was done in the time domain since this is most convenient for discontinuous functions like square pulses. It is more common to see the detector response as a function of frequency. When the incident radiation can be expressed as $W(t) = W_0 e^{j\omega t}$, the current and voltage responsivities, defined as the response divided by the input power, are

$$\mathfrak{R}_i = \left| \frac{I}{W} \right| = \frac{pAR_T\omega}{\sqrt{(1+\omega^2\tau_T^2)}} \quad , \text{ and} \quad (1.9)$$

$$\mathfrak{R}_v = \left| \frac{V}{W} \right| = \frac{pAR_T R\omega}{\sqrt{(1+\omega^2\tau_T^2)(1+\omega^2\tau_E^2)}} \quad . \quad (1.10)$$

The thermal and electrical time constants define the frequency band-

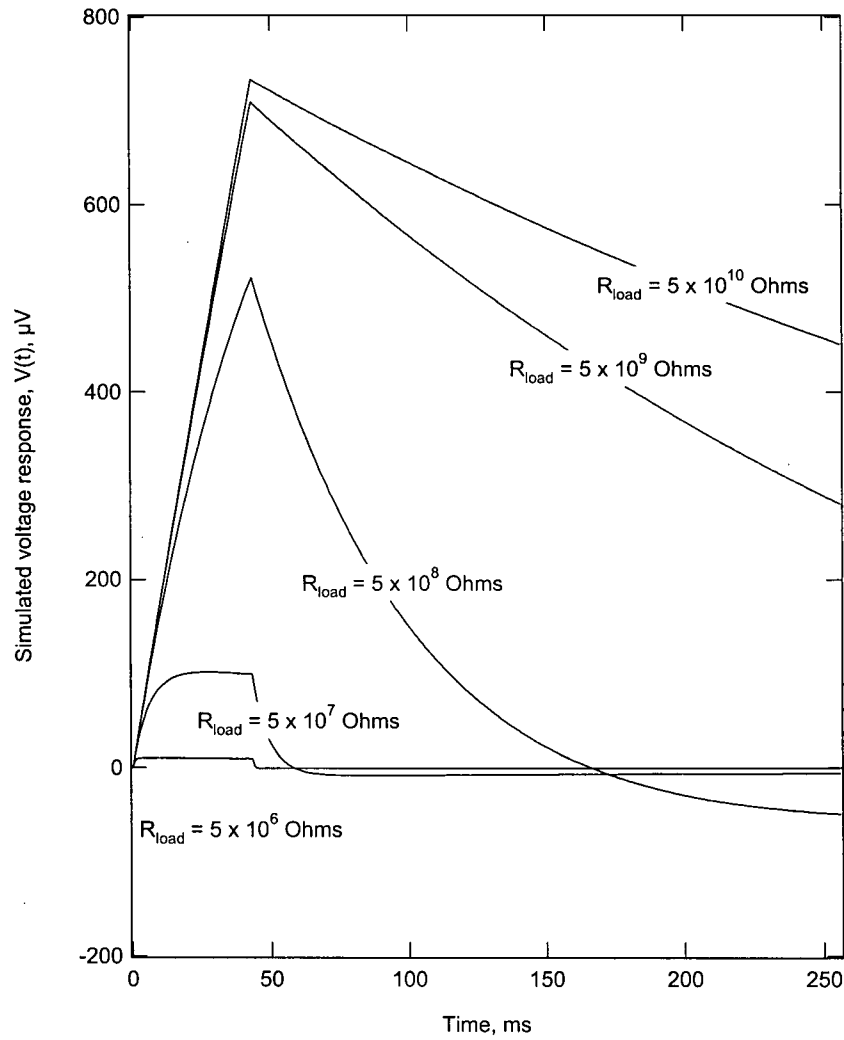


Figure 1.3: Simulated voltage response of the calorimeter for the experimental pulse conditions (256 ms, 16.6% duty) at various load resistances. The input energy was 600 nJ per pulse and the voltages are those seen across the load resistor, i.e. unamplified signal.

Table 1.2: Electrical and thermal properties of the pyroelectric sensor, comprising the lithium tantalate crystal and 500 M Ω load resistor. For derived values, the relevant equation is given in the notes column.

Property	Value	Units	Notes
Thermal Time Constant, τ_T	485	ms	measured
Heat Capacity, C_T	0.12	J/K	sv
Thermal Resistance, R_T	3.6	K/W	τ_T/C_T
Electrical Time Constant, τ_E	60	ms	measured
Total Resistance, R	500	M Ω	$= R_{load}$
Crystal Resistance	56000	G Ω	ρ_a^l
Total Capacitance, C	120	pF	τ_E/R
Crystal Capacitance	75	pF	$\epsilon_o \epsilon_l^a$

width of the responsivity. The 3 dB points are $1/(2\pi\tau_T)$ and $1/(2\pi\tau_E)$. For best performance the signal frequency should be within those limits, and the bandwidth made as small as possible by keeping the values of the two time constants similar.

1.2.4 Amplification and Signal Conditioning

In addition to the load resistance, the calorimeter detector contains a simple pre-amplifier circuit shown in Figure 1.4. The voltage follower provides no voltage gain, but it reduces the susceptibility of the output signal to noise pickup by lowering the output impedance. It consists of a 2N4117A jFET with a 100 k Ω bias resistor, R_s , on the source pin and 5 VDC applied to the drain.

The signal generated by the pyroelectric detector is attenuated slightly by the jFET follower which has a gain, A , determined by the following ex-

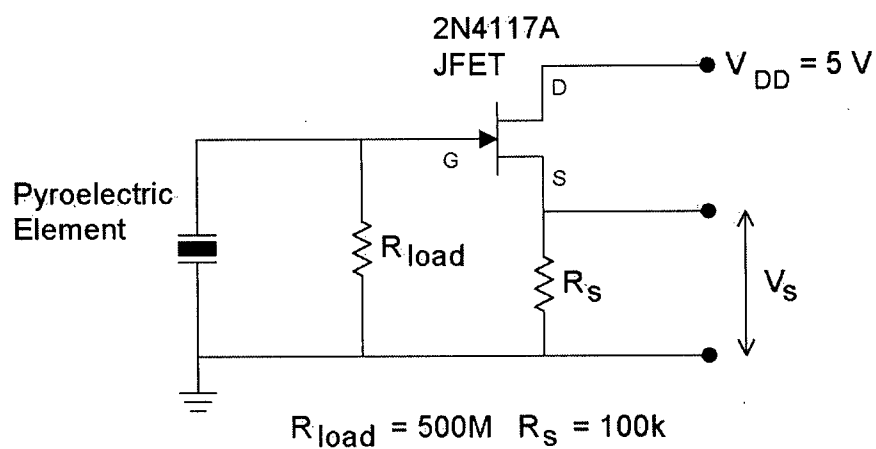


Figure 1.4: A circuit schematic of the pyroelectric detector. The pyroelectric element is in parallel with a load resistance R_{load} , and connects to the gate of the jFET source follower. The output signal, V_s , is taken across the source resistor, R_s . A 5 V bias voltage, V_{DD} , is applied to the jFET drain.

pression, [32]

$$A_{jFET} = \frac{g_{fs}R_s}{1 + g_{fs}R_s} \quad , \quad (1.11)$$

where g_{fs} is the forward transconductance of the transistor. For $R_s = 100 \text{ k}\Omega$, the calculated gain with a 2N4117A jFET is 0.93.

As this circuit is located inside the UHV chamber the components had to be selected for UHV compatibility. Glass encapsulated resistors were purchased from Ohmite (Ultra High Resistance High Stability Hermetically Sealed Resistors, 10% Tolerance). The jFET was also hermetically sealed, with a metal case. (Multiple manufacturers, Vishay etc.) All electrical connections were made with set screws or spring clips, no solder was used.

The voltage amplification was external to the UHV chamber. The circuit, shown in Figure 1.5, was developed around two Burr-Brown INA110 instrumentation op-amps. It is a dual differential design, AC coupled, with a bandwidth of 0.3 Hz to 3300 Hz. A differential gain setting of 4000 was used during all the calorimetry and calibration experiments.

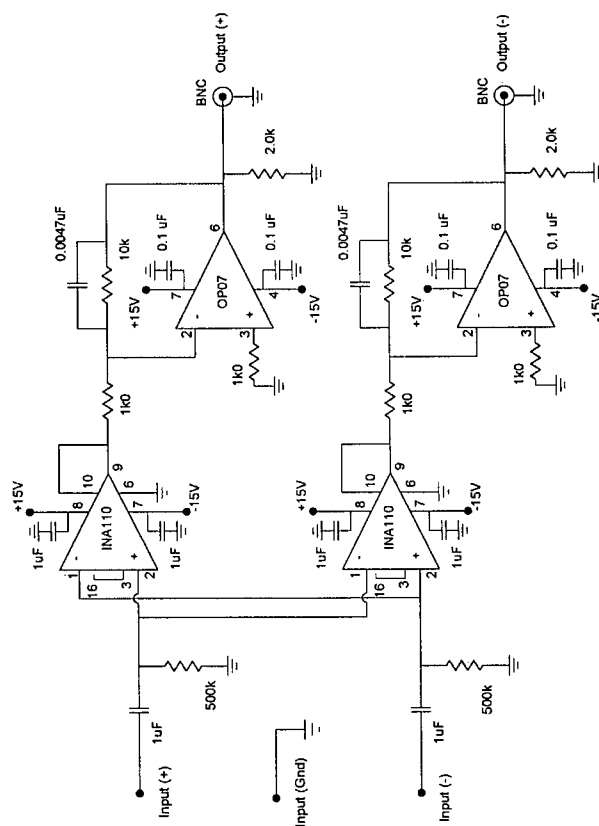


Figure 1.5: Schematic of the signal amplifier used with the pyroelectric sensor. It is a dual differential design using INA110 instrumentation op-amps. The gain is 4000.

Finally, the signal was digitized by a 16 bit A/D card (National Instruments AT-MIO-16XE-50) and streamed to disk in real time. Data acquisition and processing was done in the LabView programming environment.

1.2.5 Calibration

The sensitivity coefficient, S , is defined as the ratio of the measured height of the calorimeter signal to the incident heat input. The sensitivity of the pyroelectric sensor was calibrated by observing the calorimeter response to a pulsed laser beam of known energy.

$$S = \frac{\text{measured pulse height}}{\text{laser pulse incident energy} \times \text{sample absorbance}} \quad (1.12)$$

A laser diode operating at 640 nm was pulsed with the same pulse characteristics as the metal atom beam: 3.9 Hz rep. rate and 16.6% duty cycle. The laser pulse energy was measured with a photodiode detector, and the beam laser intensity attenuated using neutral density filters such that the absorbed energy was comparable to the magnitudes observed during the deposition experiments. Linearity is shown in Figure 1.6.

Both the voltage signal and the incident pulse energy could be obtained with better than 1% precision. Sample reflectivity was measured ex-situ using an integrating sphere and BaSO₄ reference. The uncertainty of the reflectance measurement was large, severely limiting the accuracy of the calibration. The sensitivity coefficient S was found to be 0.89 V/ μ J, $\pm 15\%$. Testing several samples with various laser intensities produced the same result, within the admittedly large experimental error.

In comparison, the theoretical sensitivity was about 3.5 times higher,

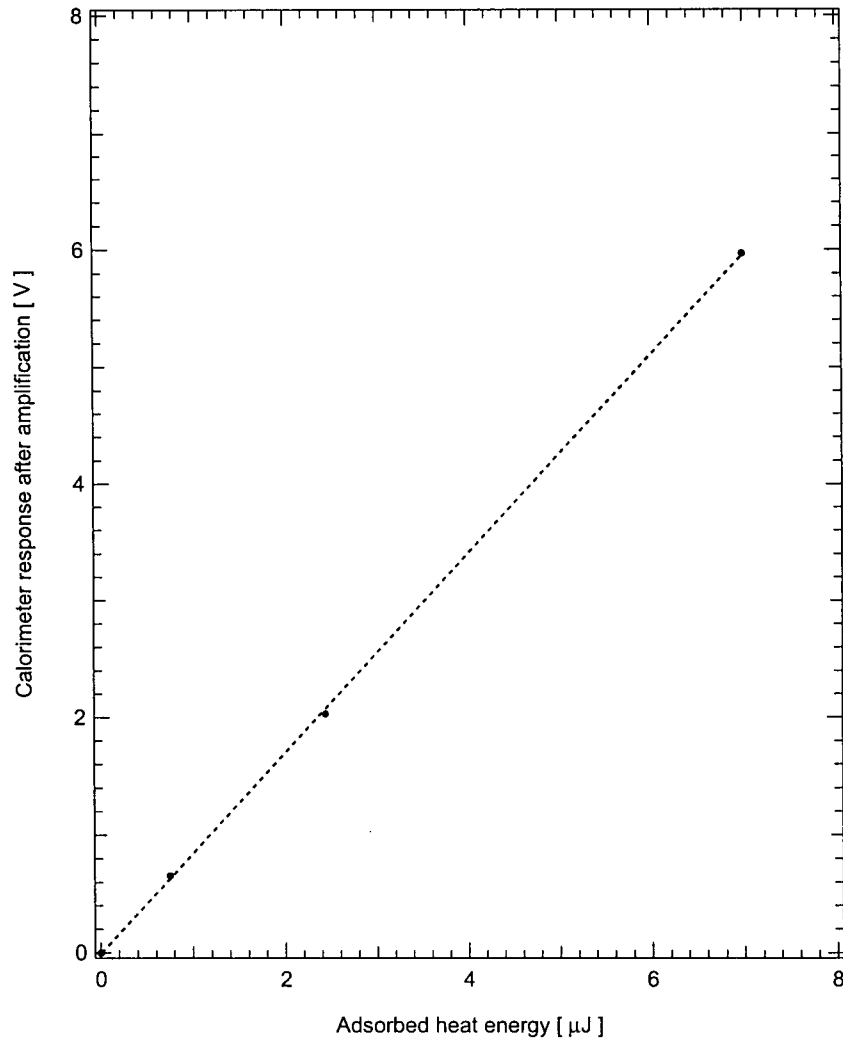


Figure 1.6: The measured calorimeter pulse heights, in response to a laser input pulse, demonstrating linearity over the energy range encountered during metal atom deposition. The gain of the amplifier was set to 4000. The sensitivity indicated by the slope of this plot is not the value used to calibrate later experiments.

3.2 V/ μ J. The discrepancy is most likely due to the uncertainty in the pyroelectric coefficient, p . A wide range of values are found in the literature, and the pyroelectric coefficient for the crystals used in the calibration and calorimetry experiments was not known.

1.3 The Metal Atom Beam

1.3.1 The Evaporation Source

The metal atoms were generated by thermal evaporation. The beam produced using this method, being essentially at thermal equilibrium, has a low kinetic energy, high stability, and low concentrations of clusters, ions, or chemical impurities. Furthermore, the kinetic energy can be calculated in a straightforward manner. (Section 1.3.3)

A high temperature evaporator and 10cc tungsten crucible purchased from Applied EPI was used with disposable alumina crucible liners from Ozark Technical Ceramics. A water filled stainless steel cooling jacket, built in-house, surrounded the crucible and heating elements.

The crucible was heated until an appreciable vapor pressure was developed over the metal sample contained within. Atoms evaporate or sublime from the metal and emerge from the mouth of the crucible in a poorly collimated stream.

See Section 2.2 for specific operating conditions.

A complete review of high temperature metal atom beam sources can be found in Ross and Sonntag [33], and includes a full table of metals and compatible crucibles.

1.3.2 The Beam Chopper

A 4 mm \times 25 mm slit placed above the mouth of the crucible allows metal atoms to pass into the part of the calorimetry chamber containing the pyroelectric detector. Directly above the slit is the beam chopper, a 50 mm wide metal disc with a single 60° notch. The disc is driven at 3.9 Hz by an external stepper motor, as shown in Figure 1.7.

The amplifier/control card (The Motion Group, model MD 1.2) used with the stepper motor could be driven by the data acquisition software. Acquisition of the calorimeter signal was synchronized to the rotation of the chopper wheel, such that each revolution of the chopper wheel, and thus one metal atom pulse, was saved to a single data array. These arrays were processed in real time to determine the signal pulse height.

The chopper speed was 3.9 Hz and the duty cycle was 16.6%, generating a square pulse train of repeat length 256 ms and 43 ms pulse width.

1.3.3 The Velocity Selector

Thermal radiation emitted from the metal atom evaporation source would overload the detection circuitry of the calorimeter if not attenuated. A velocity selector was developed with a transmission function such that thermal radiation was always blocked in the direct line-of-sight between the pyroelectric sensor and the metal atom source. The transmission of incident metal atoms was still usefully high. Through an understanding of the geometry and physics involved, detailed in the following sections, the design and operation of the velocity selector was optimized. The transmission of metal atoms was maximized and line-of-sight was blocked for the entire sample area.

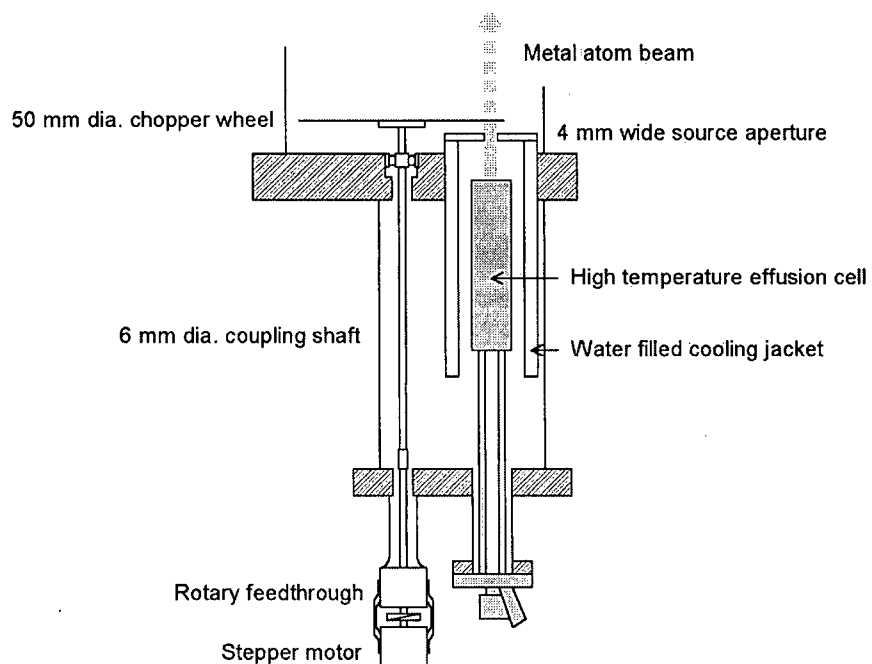


Figure 1.7: Schematic illustration of the lower part of the main UHV chamber, where the metal evaporation source, collimation aperture and beam chopper are mounted. The chopper wheel had a single 60° notch and revolved at 3.9 Hz, producing a pulsed beam with a pulse length of 256 ms and a 16.6% duty cycle.

The Slotted Disc Velocity Selector

A mechanical velocity selector creates a series of synchronized gates at various points along a particle beam. If the velocity of a particle is such that it arrives at a closed gate, it is deflected out of or otherwise removed from the beam axis. To block a line-of-sight while at the same time maximum transmission of metal atoms requires that at no point are all the gates open, but each gate is otherwise open for the longest possible time.

The slotted disc velocity selector (SDVS) is a mechanical velocity selector consisting of two or more circular discs with notches cut out around the circumference. The discs are fixed to a common axis, and rotate with an angular velocity ω . The particle beam runs parallel to the axis of rotation at a distance r away from it, such that the beam is in line with the notches on the disc. The two outermost discs are the ones that determine the transmission function, additional discs (if present) remove velocity sidebands and are not part of the parameters needed to define the operation of the selector.

Transmission Function for a Perpendicular Beam

The following derivation is closely based on methods presented in van den Meijdenberg [34] and the same variable names have been used whenever possible.

To help visualize the parameters, the circumference of each blade at “ r ” is rolled out flat, as shown in Figure 1.8. The notch width is l_1 , and the separation between notches is $l = l_1 + l_2$. All the notches must be equally spaced, thus

$$l = \frac{2\pi r}{N} = l_1 + l_2 \quad , \quad (1.13)$$

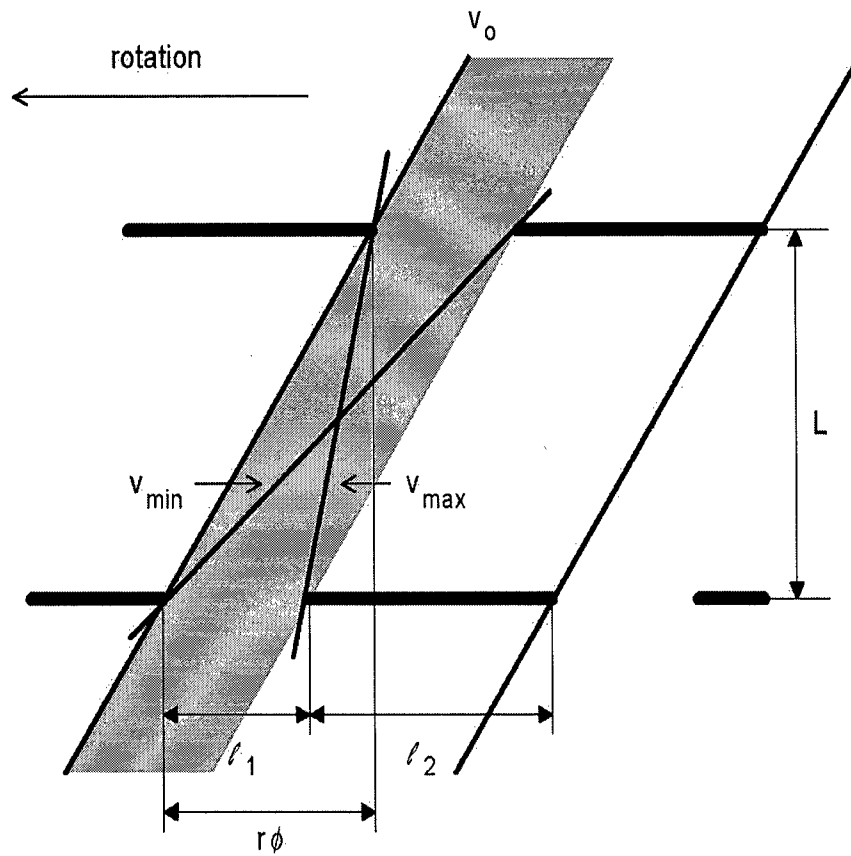


Figure 1.8: Sketch showing various parameters defining a two disc velocity selector, shown rolled out flat along the disc circumference. The heavy black lines are the two discs, which are separated by a distance L and offset by $r\phi$. ϕ is the pitch angle of the blades. The notches have a width of l_1 separated by a distance $l_1 + l_2$. Characteristic velocities through the device are indicated.

where N is the number of notches per disc. The two discs are identical, separated by a distance L and offset by a distance $r\phi$ where ϕ is the pitch, or offset angle.

The following three variables are defined,

$$\beta = \frac{z}{L} \quad , \quad (1.14)$$

$$\gamma = \frac{l_1}{r\phi} \quad , \text{ and} \quad (1.15)$$

$$\eta = \frac{l_1}{l} \quad . \quad (1.16)$$

β is the ratio of the disc thickness, z , to the separation distance, L . For the thin disc geometries under consideration this ratio is essentially zero and β may be ignored. γ is the ratio of the slit width to the offset distance. η is the duty cycle, or open fraction, of the discs.

The slope of particle trajectories drawn in Figure 1.8 is proportional to the particle velocity. The nominal velocity is determined from the slope between the leading edges of the two slots:

$$v_o = \frac{L\omega}{\phi} \quad . \quad (1.17)$$

A minimum and maximum velocity can be determined from the slopes between the leading and trailing edges,

$$v_{min} = v_o \frac{1}{1 + \gamma} \quad , \text{ and} \quad (1.18)$$

$$v_{max} = v_o \frac{1}{1 - \gamma} \quad . \quad (1.19)$$

Lastly, the the transmission function $B(v)$ - the fraction of incident to transmitted atoms - is calculated. The transmission will be dependent on

the velocity. It will be zero if $v \geq v_{max}$ or $v \leq v_{min}$. At v_o it is equal to the duty factor, η . For the other values, the available open fraction of the second notch can be determined geometrically. The result is:

$$B(v) = \begin{cases} \frac{\eta}{\gamma} \left(\gamma + 1 - \frac{v_o}{v} \right) & \text{for } v_{min} \leq v \leq v_o \\ \frac{\eta}{\gamma} \left(\gamma - 1 + \frac{v_o}{v} \right) & \text{for } v_o \leq v \leq v_{max} \\ 0 & \text{for } v \leq v_{min} \text{ and } v \geq v_{max} \end{cases} \quad (1.20)$$

Considerations for a divergent beam

The metal atom beam has an angular dispersion, due to the finite width of the sample and source. Non-perpendicular trajectories through the velocity selector must be accounted for, to confirm that line-of-sight is blocked between the source and all points on the sample as expected. Angular dispersion in the radial direction of the rotating discs has only limited effect and may be ignored, but along the tangential axis of the blades of the velocity selector, small deviations from the axis of rotation are significant.

Additional parameters for the derivation that follows are shown in Figure 1.9. The beam is defined by sample and source apertures separated by a distance, d . A test trajectory, intersects the sample aperture at a distance x from the center along an axis tangential to the blade circumference. The distance from the center of the source aperture, along this same axis, is y . The angle from perpendicular, α , of the test trajectory can be approximated by

$$\alpha(x, y) = \tan \frac{x - y}{d} \simeq \frac{x - y}{d} \quad , \quad (1.21)$$

given the usual situation where $x, y \ll r, d$. Under these conditions the arc of the blades across the sample is approximately a straight line and effects arising from the curvature of the blades can be neglected. The width of the

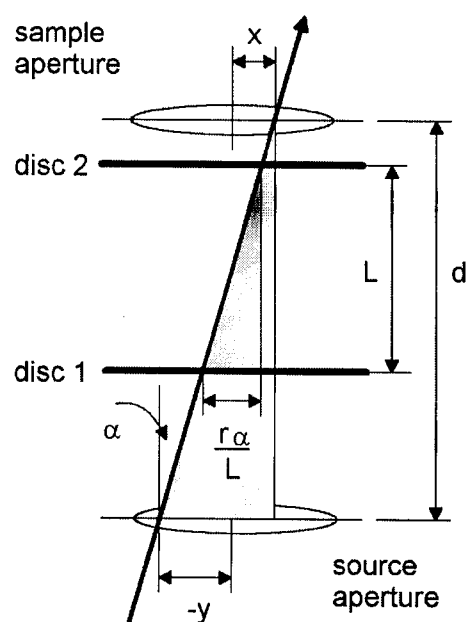


Figure 1.9: Illustrative sketch showing the additional parameters defining a non-perpendicular particle trajectory through the velocity selector.

sample and source can then be defined on the x and y ordinates as $2X$ and $2Y$ respectively, such that $-X \leq x \leq X$ and $-Y \leq y \leq Y$.

The pitch angle, ϕ , of the velocity selector is defined for a perpendicular ray. The main effect of a skewed ray is the change in apparent pitch angle, denoted $\phi'(x, y)$:

$$\phi'(x, y) = \phi + \alpha(x, y) \frac{L}{r} \quad . \quad (1.22)$$

$\phi'(x, y)$ replaces ϕ in equations 1.15 and 1.17. The usual approximation of constant γ is not appropriate in the present - unusual - case where $r\phi \sim l_1$.

The characteristic velocities become

$$v'_o(x, y) = \frac{L\omega}{\phi'} \quad , \text{ giving} \quad (1.23)$$

$$v'_{min}(x, y) = v'_o(x, y) \frac{1}{1 + \gamma'(x, y)} \quad \text{and} \quad (1.24)$$

$$v'_{max}(x, y) = v'_o(x, y) \frac{1}{1 - \gamma'(x, y)} \quad . \quad (1.25)$$

The transmission function is now

$$B'(v, x, y) = \begin{cases} \frac{\eta}{\gamma'(x, y)} \left(\gamma'(x, y) + 1 - \frac{v'_o(x, y)}{v} \right) & \text{for } v'_{min} \leq v \leq v'_o \\ \frac{\eta}{\gamma'(x, y)} \left(\gamma'(x, y) - 1 + \frac{v'_o(x, y)}{v} \right) & \text{for } v'_o \leq v \leq v'_{max} \\ 0 & \text{for } v \leq v'_{min} \text{ and } v \geq v'_{max} \end{cases} \quad (1.26)$$

In a radial plane along the axis of rotation, a similar analysis shows that divergent rays have no significant effect on the transmission function. Any point on the sample surface can therefore be characterized solely from its position along the tangential axis.

Thermal velocity distribution function

The number of metal atoms of velocity v arriving at the sample is a function of both the transmission through the velocity selector and the incident intensity.

The dependence of the incident intensity on velocity is taken up in this section.

A thermally evaporated metal vapor can be considered an ideal gas at the pressures of interest, so the speed distribution function, $f(v)$, can be expressed as a function of the molar mass, M , and temperature, T . R is the ideal gas constant, 8.314 J/mol/K. The Maxwell speed distribution function of an ideal gas is [35],

$$f(v) = 4\pi \left[\frac{M}{2\pi RT} \right]^{\frac{3}{2}} v^2 \exp \left[\frac{-Mv^2}{2RT} \right] \quad , \quad (1.27)$$

and the most probable velocity is

$$v_p = \sqrt{\frac{2RT}{M}} \quad . \quad (1.28)$$

The flux weighted velocity distribution for a ideal gas, $g(v) = vf(v)$, is the probability that a particle of a particular velocity, v , passes through a square of unit area in unit time. The expression, less constants, becomes

$$g(v) = vf(v) \propto v^3 e^{-(\frac{v}{v_p})^2} \quad , \quad (1.29)$$

which correctly represents the velocity distribution *passing into* the velocity selector. The distribution is subsequently attenuated according to the transmission function, $B'(v, x, y)$, of the velocity selector. (Section 1.3.3) Transmission functions and the flux weighted velocity distribution calculated for typical operating conditions are shown in Figure 1.10. The total transmission at any given point, x , on the sample is $T(x)$, obtained by integration over all velocities $0 \leq v \leq \infty$ and all points across the source, $-Y \leq y \leq Y$, of the product $g(v)B'(v, x, y)$,

$$T(x) = \int_y \int_v g(v) B'(v, x, y) dv dy \quad . \quad (1.30)$$

The integral is normalized to the total probability of the beam at the source aperture,

$$T(x) = \frac{\int_{-Y}^Y \frac{\int_0^\infty g(v) B'(v, x, y) dv}{\int_0^\infty g(v) dv} dy}{\int_{-Y}^Y dy} \quad (1.31)$$

The kinetic energy of the atoms after passing through the velocity selector, E_{kin} , will be transformed into heat when the atoms adsorb on the polymer sample. This heat will add to the observed calorimeter signal and must therefore be accounted for. (Section 2.4.4.) E_{kin} is calculated from the mean square velocity:

$$E_{kin}(x) = \frac{1}{2} M \int_y \int_v B'(v, x, y) g(v) v^2 dv dy \quad (1.32)$$

$$E_{kin}(x) = \frac{1}{2} M \frac{\int_{-Y}^Y \frac{\int_0^\infty g(v) B'(v, x, y) v^2 dv}{\int_0^\infty g(v) B'(v, x, y) dv} dy}{\int_{-Y}^Y dy} \quad (1.33)$$

If the width of the source aperture is small relative to the sample, the kinetic energy can be approximated by omitting the integration over y , calculating $T(x)$ and $E_{kin}(x)$ for $y = 0$ only:

$$E_{kin}(x) \approx \frac{1}{2} M \frac{\int_0^\infty g(v) B'(v, x, 0) v^2 dv}{\int_0^\infty g(v) B'(v, x, 0) dv} \quad (1.34)$$

The average kinetic energy is only a small component ($2 \sim 10\%$) of the total calorimetry signal. The calculation based on a non-divergent geometry,

$$E_{kin} \approx \frac{1}{2} M \frac{\int_0^\infty g(v) B(v) v^2 dv}{\int_0^\infty g(v) B(v) dv}, \quad (1.35)$$

was found to provide a sufficiently accurate estimate. The results are listed in Table 1.3.

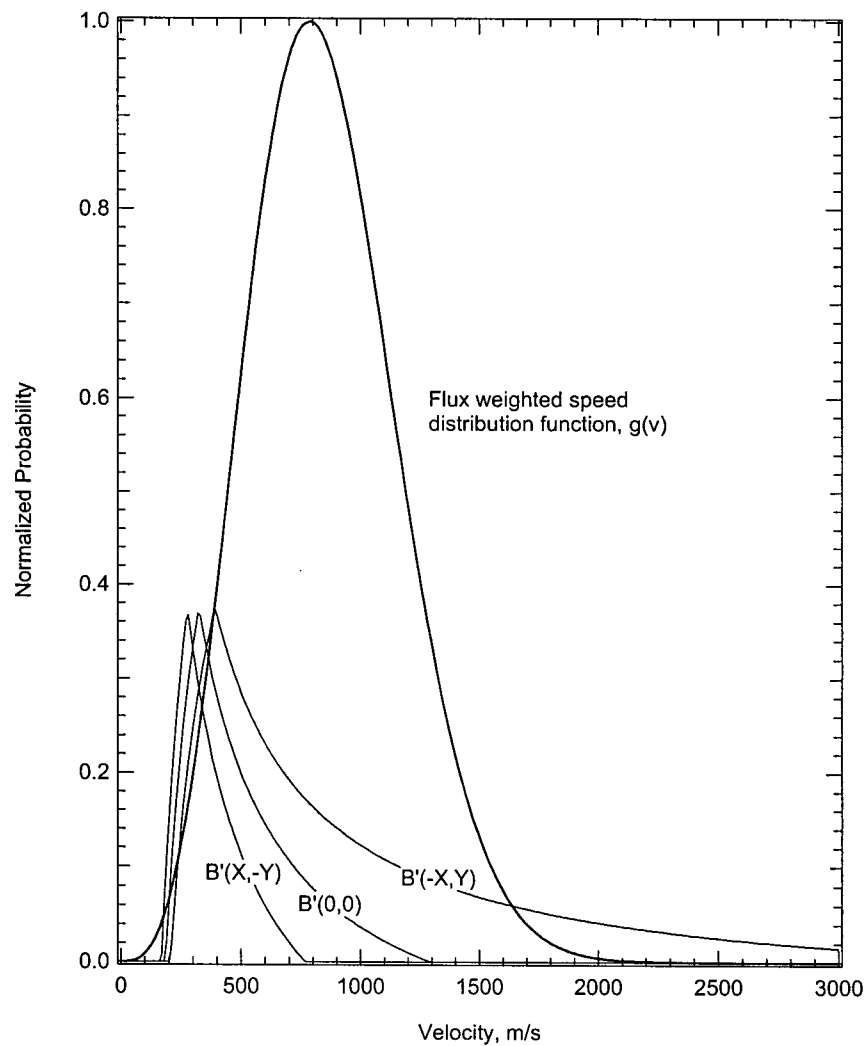


Figure 1.10: The flux-weighted velocity distribution of copper at 1300 °C incident to the velocity selector, $g(v)$, shown with the transmission functions of the velocity selector calculated for perpendicular ($B'(0, 0)$) and extreme divergent ($B'(X, -Y)$, $B'(-X, Y)$) paths through the sample and source apertures. The transmitted intensity, not shown, is the product $g(v)B'(v, x, y)$.

Table 1.3: The kinetic energy calculated using Equation 1.35 for thermally evaporated metal atom beams of copper, calcium and chromium under experimental deposition temperatures.

Element	Molar Mass M , g/mol	Evaporation Temperature T , °C	Mean Velocity v_m , m/s	Kinetic Energy E_{kin} , kJ/mol
Cu	63.55	1300	642	14.5
Cr	52.00	1700	794	14.4
Ca	40.08	575	593	9.9

Optimizing the velocity selector for maximum transmission

Line-of-sight between the source and sample apertures must not exist for any point on the sample if the velocity selector is to be effective at blocking thermal radiation. Mathematically, this is equivalent to requiring $\gamma'(x, y) < 1$ for all (x, y) , where x is the sample diameter axis, running from $-X \leq x \leq X$, and y is the source diameter axis, similarly $-Y \leq y \leq Y$.

The notch width l_1 and pitch ϕ of the velocity selector can be adjusted to insure this condition, or the beam aperture widths can be reduced.

Further reduction in $\gamma'(x, y)$ or the aperture width reduces the overall transmission. Optimal conditions are obtained by maximizing γ until just before line-of-sight exists for the worst-case divergent beam. The most convenient variable to adjust for this purpose is the notch widths, l_1 and l_2 . (Figure 1.8)

From geometric arguments the optimal values of the blade notch width and duty cycle can be expressed as,

$$l_2 - l_1 > (X + Y) \frac{2L}{d} \quad . \quad (1.36)$$

Table 1.4: Dimensions and others specifications of the slotted disc velocity selector.

Description	Value
Angular Velocity, ω	1.13 rad/ms
Blade Radius, r	50 mm
Blade Separation, L	100 mm
Notch Width, ℓ_1	13.1 mm
Pitch Angle, ϕ	.349 rad
Duty Cycle, η	.375
Sample Aperture Width, $2X$	8 mm
Source Aperture Width, $2Y$	4 mm
Aperture Separation, d	200 mm

In practice l_2 was chosen to exceed this minimum by 2 mm for ease of alignment. The full list of operating parameters for the velocity selector is presented in Table 1.4. Only l_1 and l_2 were available as widely adjustable parameters: The physical size of the device was limited by the chamber walls and the fixed distance between the beam source and detector. The angular velocity was limited to the maximum rotational speed of the motor.

The transmission of the velocity selector is at a maximum when the characteristic velocity $v'_o(x, y) \sim v_o$ is approximately equal to the most probable velocity of the incident beam, v_p . This was not possible in the present work due to the physical limits of the angular velocity ω , radius r , and blade separation L .

The transmission through the velocity selector is not continuous. With nine notches around the blade circumference, the pulse rate of the velocity selector is approximately 1.6 kHz, inducing a high frequency modulation of the metal atom beam flux over the 3.9 Hz pulses created by the beam chopper.

The frequency of this modulation is much higher than the bandwidth of the calorimeter, however, hence only the time averaged signal is recorded. The quartz crystal microbalance is similarly unaffected by this modulation and the measured flux will therefore be equivalent to the average quantity given by the transmission calculations.

The velocity selector was designed in-house; Figure 1.11 illustrates how it was assembled. A vacuum-rated brushless DC motor (RBE-00512-B11) and controller/amplifier (EC-104X) were purchased from Köllmorgen. A stainless steel, water cooled case was constructed to hold the motor and two dry-lubricated, high-temperature bearings. With water cooling the velocity selector could be operated continuously at speeds up to 200 Hz, the motor limit. It was bolted to the bottom plate of the main chamber using with Teflon and Viton washers for vibration isolation. The blades were laser cut (Brenco Manufacturing) from 18 gauge stainless steel sheet.

Figure 1.12 shows the transmission through the velocity selector as a function of the position across the 8 mm sample width, in a plane tangential to the blade circumference. Transmission is higher on one side of the center-point than the other because there is on average a larger effective overlap, ϕ' . The effect is significant because of the large angles encountered and the less-than-optimum angular velocity, ω . The coverage on the sample at the extreme edges is $\pm 50\%$ that of the center. Fortunately this gradient only exists along the axis tangential to the rotating discs. (Section 1.3.3) As the sample is circular the majority of the sample area is concentrated at the center. About 65% of the area has a coverage gradient of less than $\pm 25\%$ and, since the gradient is nearly linear, the high and low flux sections will tend to

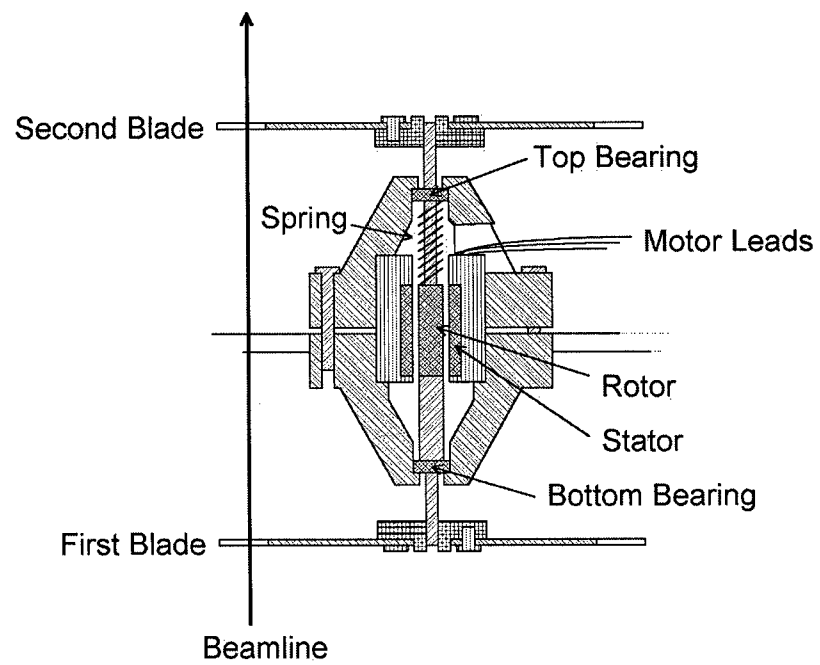


Figure 1.11: An illustration of the velocity selector, showing the motor, bearings and central shaft within the water cooled stainless steel case.

average out. The net effect can be shown to cause only a slight smoothing of features encountered in the reaction enthalpy *vs.* coverage data.

The velocity selector as a beam switch

The calculated transmission through the velocity selector exhibits a linear dependence with blade angular velocity above a certain threshold value. As shown in Figure 1.13, below a threshold rotational speed of 40 Hz the transmission is essentially zero. Thus, the atom beam flux arriving at the sample can be quickly "switched off" by reducing the motor speed below this threshold. The background signal recorded by the calorimeter in the absence of metal deposition can be monitored conveniently using this feature. Background measurements were taken at several points during the deposition experiments, and extrapolated as a continuous baseline that was subtracted from the remaining data points to give the true calorimetry signal due to the interfacial reaction.

A background signal originated from reflected light and thermal radiation from the evaporation source that reached the detector even with the velocity selector in place. A fraction of this radiation was modulated by the beam chopper in the same manner as the atom beam, adding indistinguishably to the calorimetry signal.

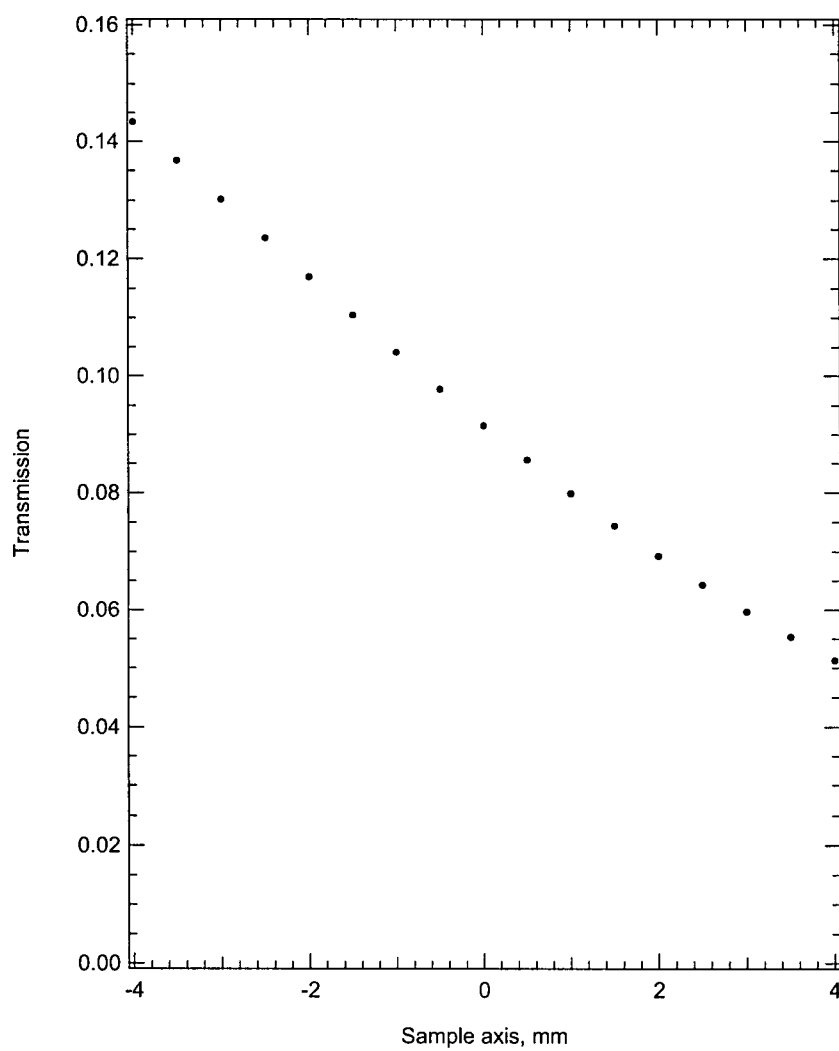


Figure 1.12: Calculated flux gradient across the sample width for a copper atom beam evaporated at 1300 °C

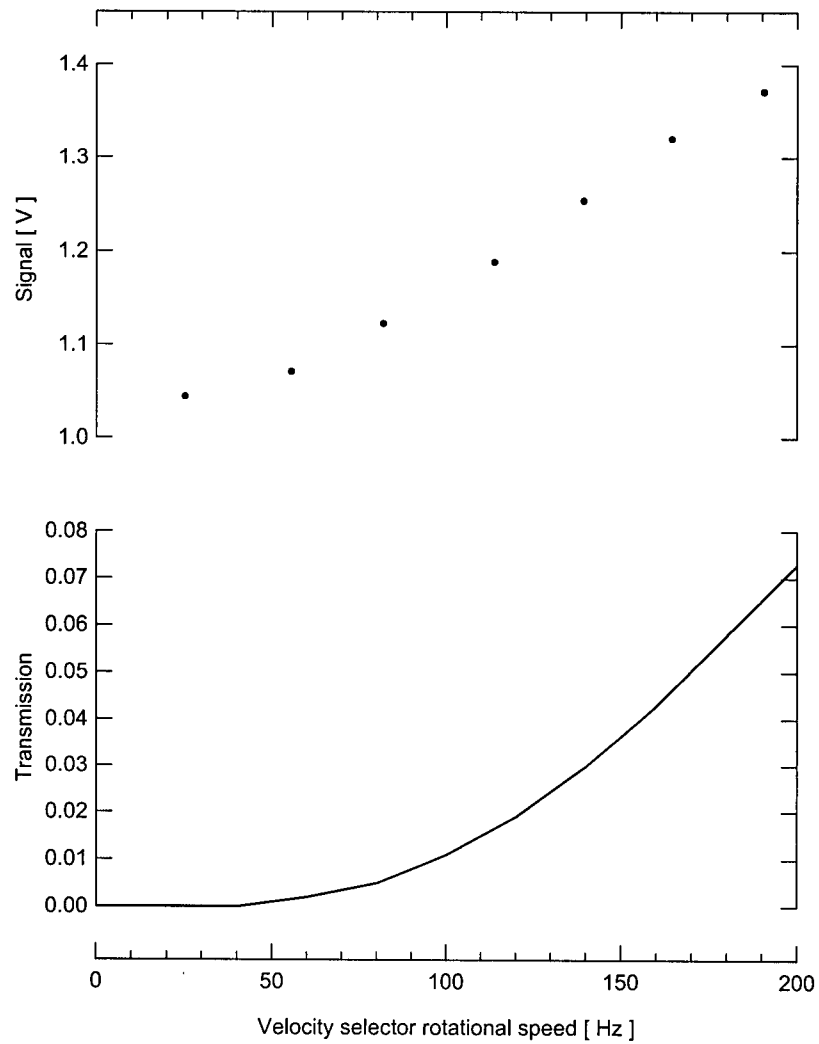


Figure 1.13: The observed calorimetry signal (top) and simulated transmission (bottom) for chromium at 1700 °C plotted against the rotational speed of the velocity selector. The transmission is effectively zero below 40 Hz.

1.3.4 Stability of the Metal Atom Beam Flux

The quartz crystal microbalance (Inficon XTM/2 with standard sensor) was periodically moved into the atom beam to check the intensity of the flux. Due to the gradient in the beam flux, discussed in Section 1.3.3, the measurement was not considered accurate enough to use in the calculation of absolute molar enthalpies. Some measure of the stability of the evaporation source over the duration of an experiment could be obtained, however, by recording the measured deposition rate before and after the calorimetry experiment.

Higher evaporation temperatures resulted in larger metal fluxes but reduced stability. The signal to noise ratio of the calorimeter signal improved, but the difference in flux at different points during a deposition experiment became unacceptably large. The deposition temperatures used were empirically found to be the best compromise.

1.4 Sample Management

The polymer film was prepared by spin-coating directly on to the front face of the lithium tantalate crystal. The crystal was then mounted within the body of a small copper stub, held in place by a screw cap. The external dimensions of the stub were compatible with a standard ESCA Mk. I sample mount, and the same system of spring-loaded forks and sockets were used to transfer the sample mount between preparation and analysis chambers. It was a convenient and rugged way to move the polymer sample. However, since the pyroelectric crystal was also contained within the stub while the rest of the signal preamplifier was located on the calorimeter station, provision had to

be made for the necessary electrical connections to complete the circuit. As shown in Figure 1.14, an internal electrode, insulated by Macor spacers from the body and cap, made contact with the back electrode of the crystal. The cap presses against the front electrode. When the stub was docked in the calorimetry station, spring clips leading to the load resistance made contact with the body and back electrode of the stub, completing the circuit.

The heating station, located in the preparation chamber, comprised a copper block with a 6 mm diameter hole to accept the sample stub and a button heater pressed against the base. A thermocouple was fitted into the side of the block. In testing temperatures of up to 600 °C were obtained with no significant temperature lag between the block and the most remote point of the sample stub.

1.5 The Ultrahigh Vacuum Environment

The calorimeter operated under UHV. The stainless steel chamber was divided into two sections by a gate valve. The metal atom beam source, mass spectrometer, and calorimeter were in the main chamber, where UHV was maintained by two ion pumps. Pressure was monitored by the readout on the ion pump controller, an ion gauge was briefly installed to confirm its accuracy. A turbo pump backed by a rotary pump was connected to the preparation chamber that contained the heating station to cure and degas the sample.

While the preparation chamber was brought to atmosphere each time a new sample was loaded, during normal operation the calorimeter chamber was kept under UHV. If the main chamber was brought to atmosphere, to

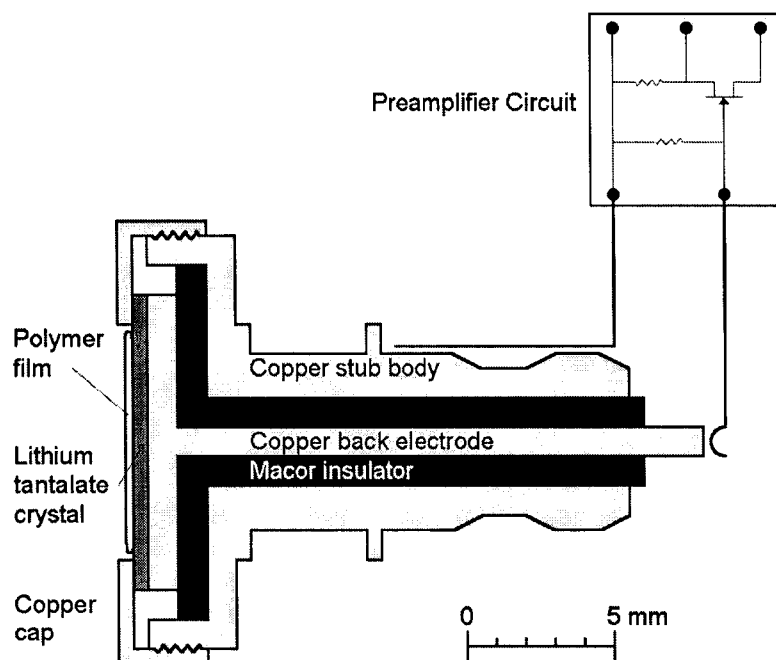


Figure 1.14: An illustration of the copper stub to which the pyroelectric element is mounted. The external design is based on the ESCA Mk. I sample mount. The internal arrangement of electrodes and insulating spacers allow the necessary electrical connections to be made between the lithium tantalate crystal and an external electric circuit.

replenish the metal in the evaporation cell for example, the entire chamber was subsequently baked at 125°C overnight.

The best base pressure was about 2×10^{-9} Torr. The evaporation source, the velocity selector, and to a lesser extent the beam chopper all contributed to the gas load when operated, such that the pressure during the deposition experiments was routinely about 2×10^{-8} Torr. The residual gas analysis is shown in Figure 1.15. Hydrogen is the most common species, and the second largest signal at 28 amu a combination of carbon monoxide and nitrogen. Hydrogen and carbon monoxide are typical outgassing products from stainless steel UHV chambers.

Contamination of the surface by the residual gases was a concern, since water vapor and oxygen, in particular, have been shown to have a significant effect on the growth of metal-polyimide interfaces. [36-39] Fortunately, although the total pressure during deposition was relatively high, the mass spectrum shows that the partial pressures of water and oxygen were much lower, accounting for perhaps three percent of the total. At 6×10^{-10} Torr these vapors are not expected to significantly affect the metal deposition reaction: at this partial pressure less than one tenth of a monolayer would impinge on the surface during a typical calorimetry experiment.

The adsorption enthalpies measured before and after periods where the flux was suspended remained constant, a good indication that residual gases do not substantially react with the metal overlayer. Nor is it expected that residual gases develop any appreciable coverage on the polymer surface, as the binding enthalpy for such interactions is expected to be small. [40] It can thus be concluded that while residual gases must always be considered as a

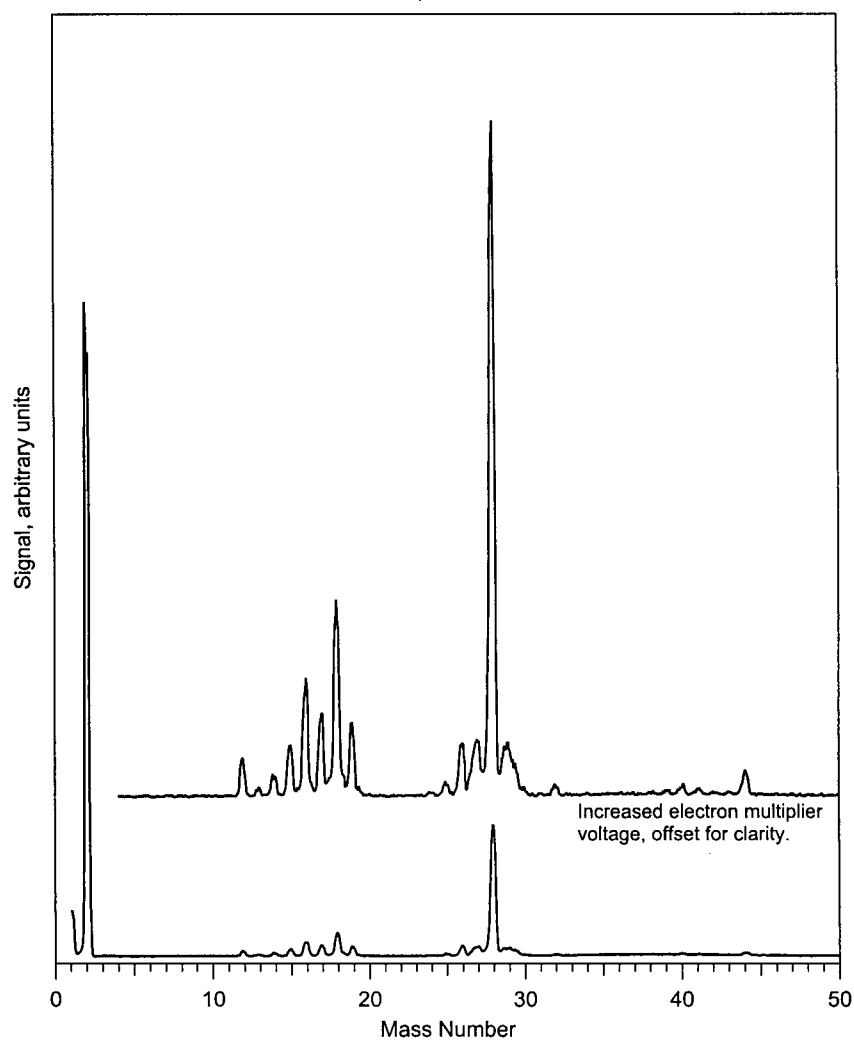


Figure 1.15: A typical mass spectrum of the residual gases in the main UHV chamber. The pressure is approximately 1×10^{-8} Torr. Hydrogen is the most prominent component.

Table 1.5: Standard deviation of the calorimeter pulse heights recorded after amplification, under standard experimental conditions except for the metal atom source which was at room temperature.

Noise σ	Motor Speeds		Amplifier	
	Velocity Selector	Beam Chopper	Input Connection	Power
0.127 mV	178 Hz	3.9 Hz	Connected to Detector	On
0.153 mV	44 Hz	3.9 Hz	Connected to Detector	On
0.093 mV	Off	3.9 Hz	Connected to Detector	On
0.019 mV	Off	Off	Connected to Detector	On
0.010 mV	Off	Off	Shorted	On
0.000 mV	Off	Off	Shorted	Off

potential source of interference, it is unlikely that this had any significant effect on the calorimetry experiments presented in this work.

1.6 Vibration Control and Noise

Lithium tantalate is both a pyroelectric and piezoelectric material: deformation of the crystal generates charge, and this deformation can be induced by either mechanical or thermal stress. The same electrical circuitry that amplifies the heat signal also amplifies the noise induced by mechanical vibrations, making the calorimeter detector vibration sensitive. As the data in Table 1.5 shows, vibrations from the velocity selector and beam chopper were the dominant noise sources. These devices, when operating, increased the noise by an order of magnitude. It is seen in the table that the noise was lower when the velocity selector was run at higher speed. This was likely the result of the fundamental resonant frequency of the beam chopper moving further away from the detector bandwidth.

In comparison, the noise introduced by the amplifier, external cabling, and analog to digital conversion is of little consequence. The high impedance part of the electrical circuit, principally the load resistor, was sensitive to noise pickup from capacitative coupling as well as being microphonic. An electrostatic screen around the preamplifier circuit reduced some of the interference. The main concerns, however, were the beam chopper and velocity selector. In an effort to isolate and damp these noise sources the velocity selector was mounted on teflon/rubber grommets and the stepper motor used to drive the beam chopper was held away from the chamber by flexible Lexan plates.

Experimental

This chapter documents the procedures and techniques used to perform the calorimetry experiment, in which Ca, Cr and Cu are deposited on PMDA-ODA polyimide substrates. The apparatus is described in the previous chapter. The preparation of the polymer sample and metal evaporation source is given, along with the procedures for transforming the data from peak height voltages to adsorption enthalpies.

2.1 Preparation of the Polymer Substrates

PMDA-ODA Polyimide films were formed directly on the gold coated lithium tantalate substrate by spin-coating. When a drop of solution of polyamic acid in N-methyl pyrrolidone (NMP) was placed on the spinning lithium tantalate disc, it immediately spread out to evenly coat the entire surface. The sample was heated in air at 100 °C for about half an hour to evaporate most of the solvent, after which the crystal was mounted in the copper sample stub and placed in the preparation section of the UHV chamber. (See Section 1.4 of Chapter 1 for details on sample manipulation.)

The sample was heated under UHV to 400 °C. This curing step condensed the polyamic acid, forming the polyimide product. (Figure 2.1) The heating was done gradually, in a series of 4 °C/min ramps to 100, 200, and finally 400 °C to ensure the NMP solvent was removed well before the condensation

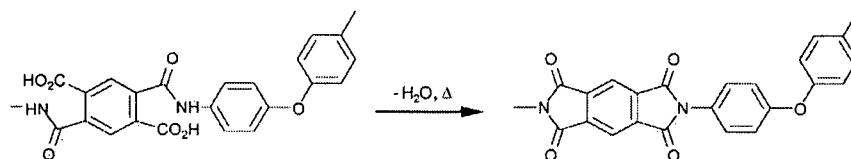


Figure 2.1: Condensation reaction of the polyamic acid precursor to form pyromellitic dianhydride oxydianiline (PMDA-ODA) polyimide polymer.

takes place. At 400 °C complete imidization is expected. A full discussion of polyimide curing methodology can be found in Coburn and Pottiger [41].

Provided the deposition experiment was to take place within one day of the curing the sample, no further preparation was done. If the sample was removed from the chamber, or left under vacuum for an extended period of time, it was degassed at 200 °C for several hours before use.

The thickness of the polyimide films was about 1 μm , determined by profilometry. The RMS roughness, determined from AFM measurements of a 50 μm line section, was found to be 300 nm, approximately the same as the roughness of the underlying substrate.

2.2 Preparation of the Metal Atom Beam

Copper (Kurt J. Lesker, 99.99%), calcium (Alfa Aesar, 99.5%) or chromium (Alfa Aesar, 99.98%) metal was used. The deposition temperatures were 1300 °C, 575 °C and 1700 °C, respectively.

To load a new charge of metal, a new alumina liner is first degassed under UHV at about 100 °C above the expected deposition temperature. The liner

is then filled about one third full with metal, and the system is again degassed by heating to a temperature close to the expected deposition temperature for several hours or until the base pressure has stabilized.

Typical ramp rates of 5 °C/min were used at low temperature, slowing to 1 °C/min near the metal melting point. With molten metal, faster heating rates of up to 10 °C/min could be used. Excessive ramp rates can cause the alumina crucible liner to fracture.

2.3 Procedures for Running a Calorimetry Experiment

It took several hours to bring the evaporation source up to deposition temperature. (Section 2.2) The sample was meanwhile moved from the preparation chamber to the calorimeter station in the main chamber. The electronics for the beam chopper, velocity selector and pyroelectric sensor were powered up and tested. The microbalance was moved into position to monitor the beam flux. This also blocked the sample from the atom beam, preventing accidental metal contamination.

The beam flux was monitored by the microbalance with the beam chopper disc stationary in the open position and the velocity selector set to high speed. After successive readings confirmed that the flux was stable, control was passed to the software. The data acquisition program controlled both the velocity selector and the beam chopper. Initially the software set the chopper to 3.9 Hz and the velocity selector to low speed.

At this point the microbalance was moved out of the atom beam, and data acquisition began. Typically 1000 revolutions of the chopper were recorded

with the velocity selector running at low speed, followed by 2000 at high speed. Each revolution of the chopper produced a single metal atom pulse. At low speed transmission through the velocity selector was zero and the recorded signal was the result of infrared radiation only. At high speed metal atoms passed through the velocity selector (adding a high frequency modulation to the flux that was subsequently time-averaged by the calorimeter detector) and deposited on the polymer sample. This cycle was repeated until sufficient metal had been deposited, at which point the acquisition program was terminated, the beam flux once again measured using the microbalance, and finally the evaporation source cooled to idling temperature. The data acquisition took about one hour for a typical experiment of approximately 15000 recorded pulses.

2.4 Treatment of Raw Data

2.4.1 Pulse Height Measurement

An array of 500 samples was read from the output of the pyroelectric detector for each revolution of the beam chopper disc i.e. one metal atom pulse. The pulse height was measured as the difference between two averaged sections of the 500 point data array, one centered on the peak maximum and the other on the flat section before the initial rise. The two sections were 40 points wide, separated 100 points apart.

Pulse height data can be averaged together to reduce scatter at the expense of coverage resolution. For the data shown in this work one hundred pulse heights were averaged together before the data was stored for later analysis. Averaging pulses reduced the number of data points for a single

experiment from 15000 to 150, with a tenfold reduction in scatter.

2.4.2 Subtraction of the Optical Baseline

Optical radiation from the hot metal atom source passing through the beam chopper added to the recorded heat signal. While the velocity selector attenuated this interference, it did not eliminate it completely.

When the atom beam flux was reduced to near-zero by lowering the speed of the velocity selector from 173 Hz to 44 Hz, only radiation contributes to the signal. By sampling the baseline in this manner at several points during the experiment, the magnitude of the optical signal could be estimated by interpolation, and subtracted from the data points recorded during metal deposition.

The averaged pulse height data contains sections where the atoms are transmitted through the velocity selector, as well as sections where the flux was cut off to monitor the optical baseline signal. The file was parsed manually to extract the points coinciding with metal atom deposition from which an interpolated baseline was subtracted.

For the calcium and copper experiments the baseline changes were small relative to the frequency of baseline measurement, so a linear interpolation was adequate. (Figures 3.1 and 3.5) The radiation signal was much larger for the chromium data due to the higher deposition temperatures required and furthermore changed rapidly with increasing metal coverage. (Figure 3.3) For the chromium results, where large differences were frequently observed between successive measurements of the baseline signal, the baseline was taken to be a proportion of the total signal as determined by the baseline-

to-signal ratio at the endpoints of each section of baseline data. The ratio was extrapolated linearly between baseline measurements. Since the baseline made up more than 90% of the total this procedure, while far from ideal, was considered satisfactory.

2.4.3 Conversion to the Calorimetric Molar Heat

Once the optical signal has been subtracted the data file becomes an array of points in sequential coverage increments containing voltages due to the metal deposition signal only. To calculate the heat of reaction, q , the voltages are converted to heat energy. The amount of heat released during the coverage increase is

$$q = \frac{\text{averaged pulse height} \times \text{number of pulses averaged}}{S} \quad (2.1)$$

The sensitivity coefficient, S , was determined by calibration to be $0.89 \text{ V}/\mu\text{J}$. (Section 1.2.5)

The molar heat of reaction for a finite step coverage increase, q_{cal} , is the heat evolved, q , divided by the number of moles of metal atoms, n , deposited in the interval

$$q_{cal} = \frac{q}{n} \quad (2.2)$$

A calibrated quartz crystal microbalance has been used in a similar experiment [14] to measure n , but in the present instance the inability to accurately position the microbalance coupled with a flux gradient inherent to the operation of the velocity selector made it difficult to obtain measurements of the absolute atom beam flux using the microbalance. The coverage increase is instead calibrated to an internal standard. n is determined from q at a point

where the molar heat of reaction, q_{cal} , can be determined by independent appeals to available literature data. (For instance reference [42].)

The most convenient is bulk heat of condensation, which is expected to be returned by the calorimeter at high metal coverages where metal-on-metal deposition occurs. [14]

2.4.4 Conversion of the Measured Enthalpy to Standard Conditions

The molar heat of reaction q_{cal} is not measured for the thermodynamic standard state. If the experiment was performed under standard conditions of 1 atm and 298 K, then the measured heat would equal the change in enthalpy, ΔH , and this enthalpy would be directly comparable to the such standard quantities as the bulk enthalpy of condensation, tabulated bond energies, etc. [14] As the experiment is performed under UHV conditions and furthermore the energy of the metal atoms is defined by their translational kinetic energy rather than by their temperature, the measured heat q_{cal} differs from what would be measured under standard conditions - termed the heat of adsorption q_a - by a small factor equal to the kinetic energy of an ideal gas at 298K, $3/2RT$, and the energy required to compress the gas to zero volume at standard pressure, RT , minus the kinetic energy of the beam, E_{kin} ,

$$q_a = q_{cal} + \left(\frac{5}{2}RT - E_{kin} \right) \quad . \quad (2.3)$$

The kinetic energy of the atom beam, calculated using Equation 1.35, is listed for the three metals in Table 1.3.

2.4.5 Conversion from Differential to Integral Enthalpy

For the general case where $\Delta H(N)$ is the reaction enthalpy of N moles of reactant the integral heat, $\Delta H_{\text{int}}(N)$, and the differential heat, $\Delta H_{\text{diff}}(N)$, are given by

$$\Delta H_{\text{int}}(N) = \frac{\Delta H(N)}{N} \quad , \text{ and} \quad (2.4)$$

$$\Delta H_{\text{diff}}(N) = \frac{d\Delta H(N)}{dN} \quad . \quad (2.5)$$

As the calorimeter measures the heat in discrete coverage increments, the calculated reaction enthalpies approximate differential quantities. For the data analysis it is sometimes necessary to convert from differential to integral enthalpies. The mathematical relation is derived by integrating Equation 2.5, followed by substitution of Equation 2.4,

$$\Delta H_{\text{int}}(N) = \frac{1}{N} \int_0^N \Delta H_{\text{diff}}(x) dx \quad . \quad (2.6)$$

For a finite number of data points with a constant spacing n the integral can be replaced by the following sum,

$$\Delta H_{\text{int}}(N) = \frac{n}{N} \sum_{x=0}^N \Delta H_{\text{diff}}(x) \quad . \quad (2.7)$$

Expressed for the i^{th} data point the integral heat is,

$$\Delta H_{\text{int}}(N_i) = \frac{n}{N_i} \sum_{j=1}^i \Delta H_{\text{diff}}(N_j) \quad . \quad (2.8)$$

Results

3.1 Calcium, Copper and Chromium Deposition on Polyimide

Calcium, copper, and chromium were deposited on PMDA-ODA polyimide substrates while the calorimeter recorded the reaction heats as a function of metal coverage. The results of these experiments are shown here. Both the “raw” data - the averaged pulse heights before the subtraction of the optical baseline - and the derived plots of reaction enthalpy *vs.* metal coverage are presented. The experimental conditions are summarized in Table 3.1.

Table 3.1: Conditions and parameters needed for the analysis of the calcium, chromium and copper calorimetry data.

	Calcium	Copper	Chromium
Date Code	020227	010725	010511
Sample Temperature	Ambient Conditions, 25°C		
Metal Source Temperature	575 °C	1300 °C	1700 °C
$q_a \rightarrow q_{cal}$ [kJ/mol]	-3.7	-8.3	-8.2
$-\Delta H_{\text{bulk}}$ [kJ/mol]	177.8	337.4	397.5
Measured Atom Flux [nm/min]	0.65→ 0.38	0.39	0.56
Calibrated Atom Flux [nm/min]	0.43→ 0.25	0.33	0.49
Detector Sensitivity, S	0.89 V/ μ J		

3.1.1 Calcium on Polyimide

Since calcium was evaporated at a relatively low temperature of 575 °C, the optical signal was small compared to the adsorption signal. (Figure 3.1) It was almost constant over the length of the experiment and was subtracted without difficulty. The beam flux, however, decreased by 40% over the duration of the experiment. This was determined from the microbalance readings before and after the deposition. The coverage step increment was scaled proportionally, taking the decrease in flux to be linear.

The appropriateness of this measure is seen by noting that the signal heights exhibit no sharp breaks or anomalous shifts, instead the final part of the deposition signal is linear with a slope corresponding to the calculated rate of decrease. When the signal is divided by the scaled coverage increments to give the molar enthalpy, the signal decays to a horizontal asymptote. (Figure 3.2)

The constant enthalpy above 1 nm calcium coverage was taken to be 177.8 kJ/mol, the bulk heat of metal condensation. This reference was used to calibrate the absolute intensity of the metal atom beam. (Section 2.4.3)

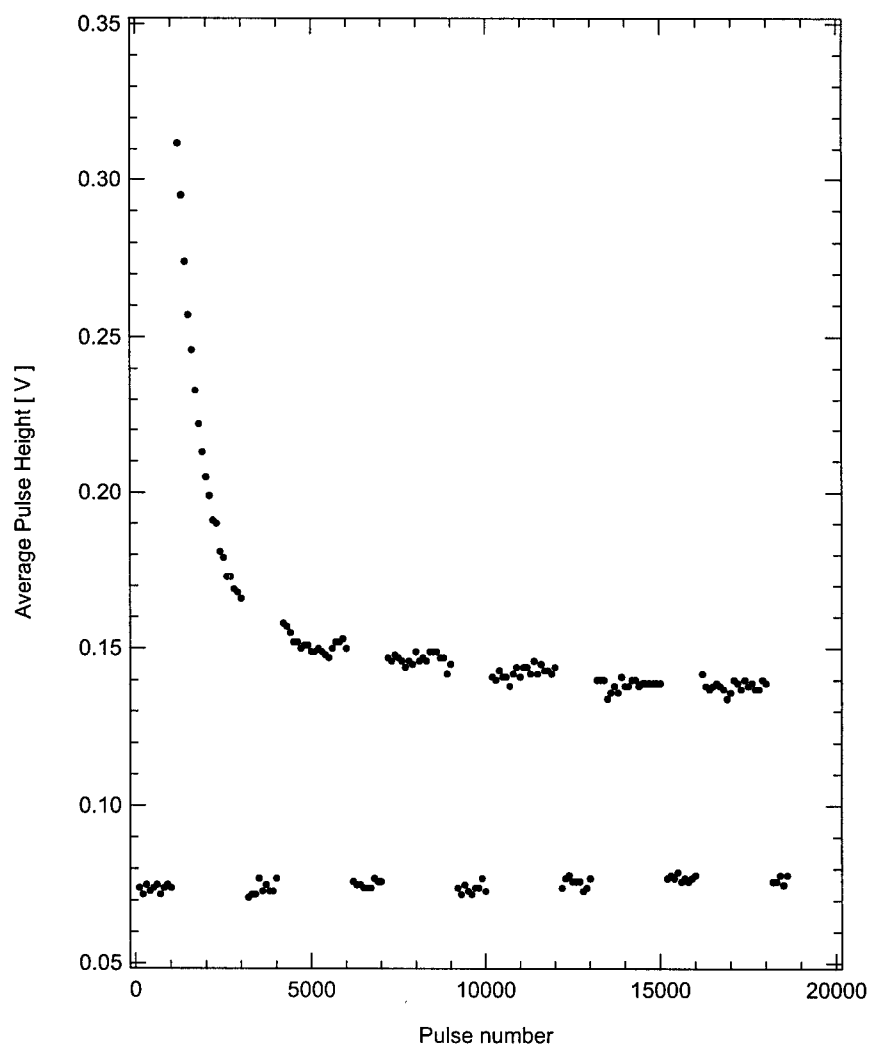


Figure 3.1: Calorimeter signal pulse heights obtained for calcium deposited on polyimide. Each data point is an average of 100 pulses. Metal deposition was suspended seven times during the experiment to determine the intensity of the optical background signal, indicated by the seven sections of data below 100 mV.

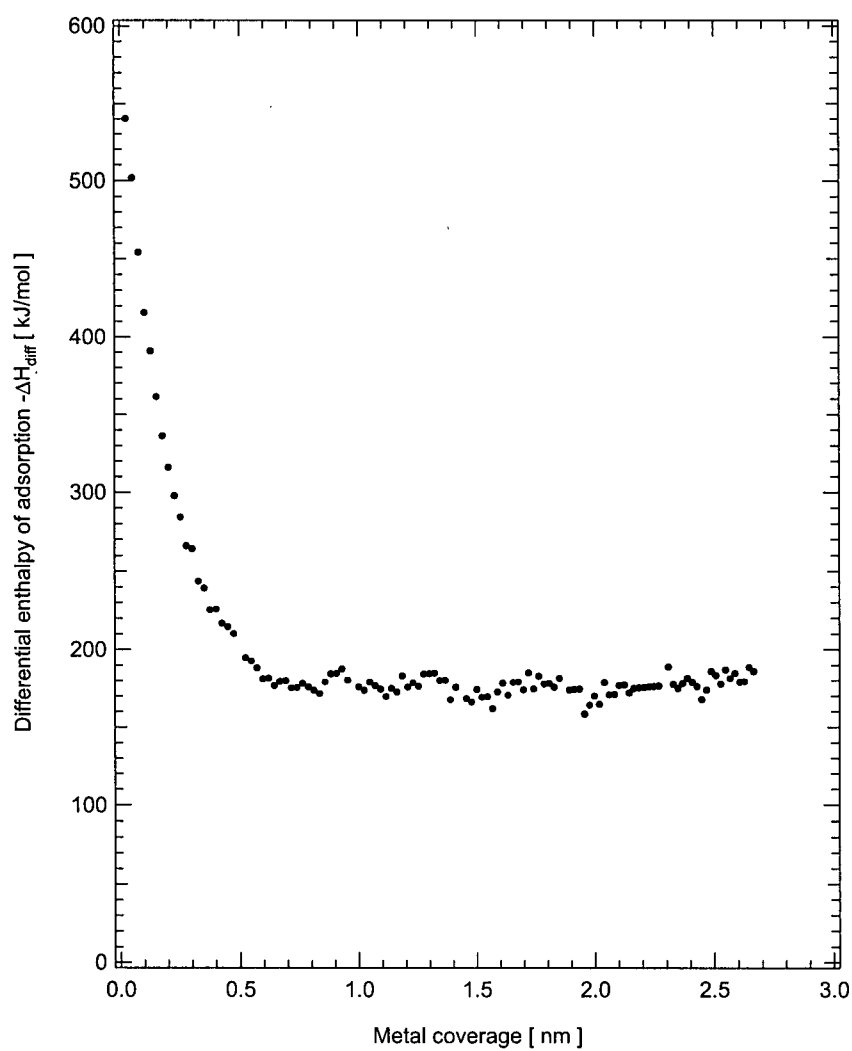


Figure 3.2: Differential enthalpy of reaction $-\Delta H_{\text{diff}}$ for calcium deposited on polyimide, reported as a function of calculated metal coverage.

3.1.2 Chromium on Polyimide

The deposition of chromium was notable for the high crucible temperatures required to produce sufficient atom beam flux. At 1700 °C the optical signal was significantly larger than that resulting from metal adsorption. The flux was particularly stable over the course of the experiment, presumably because at this deposition temperature, chromium metal is still solid. The vapor is produced by sublimation rather than evaporation.

The thermal background and the adsorption heats displayed similar behavior. Both remained low during the early deposition stages, then rose sharply. The heat signal quickly levelled off to a constant value assigned to 397.5 kJ/mol, the bulk heat of metal condensation. This reference was used to calibrate the metal atom beam flux. The optical signal continued to rise slightly.

See Figure 3.3 for the complete pulse heights, and Figure 3.4 for the plot of reaction enthalpy *vs.* metal coverage.

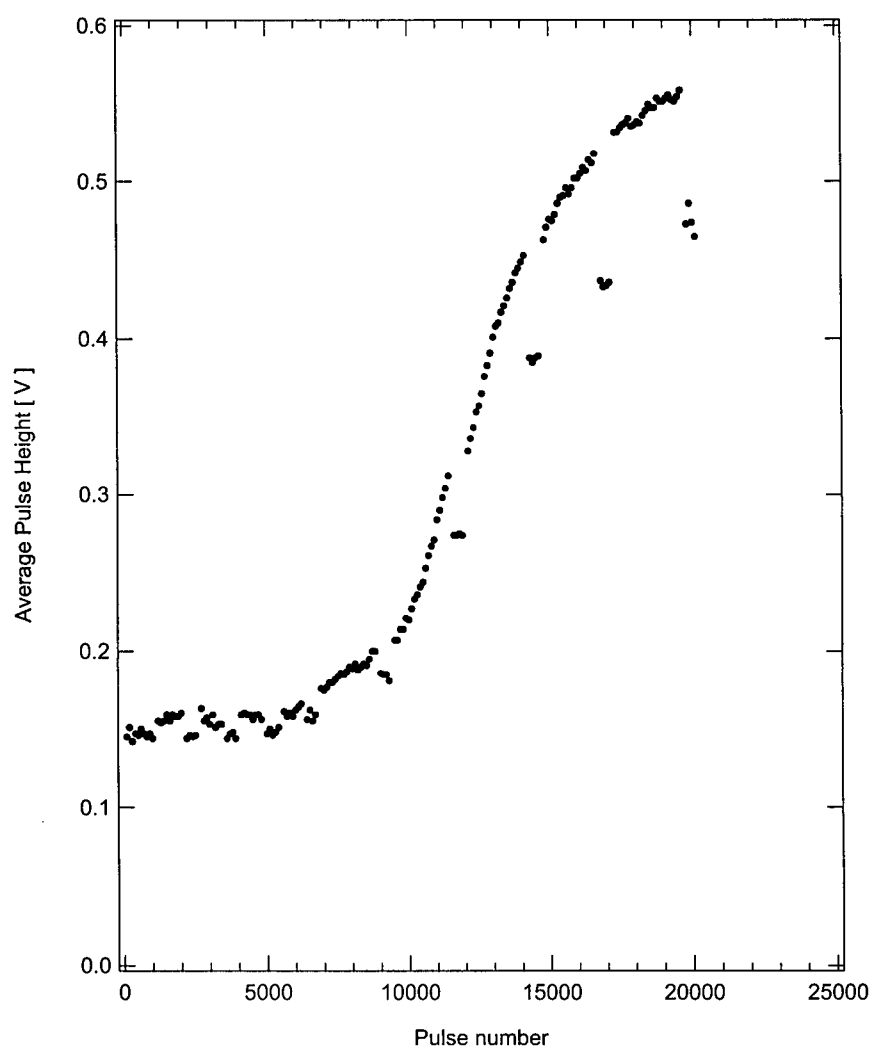


Figure 3.3: Calorimeter signal pulse heights obtained for chromium deposited on polyimide. Each data point is an average of 100 pulses. Metal deposition was suspended at several points during the experiment to determine the optical background signal.

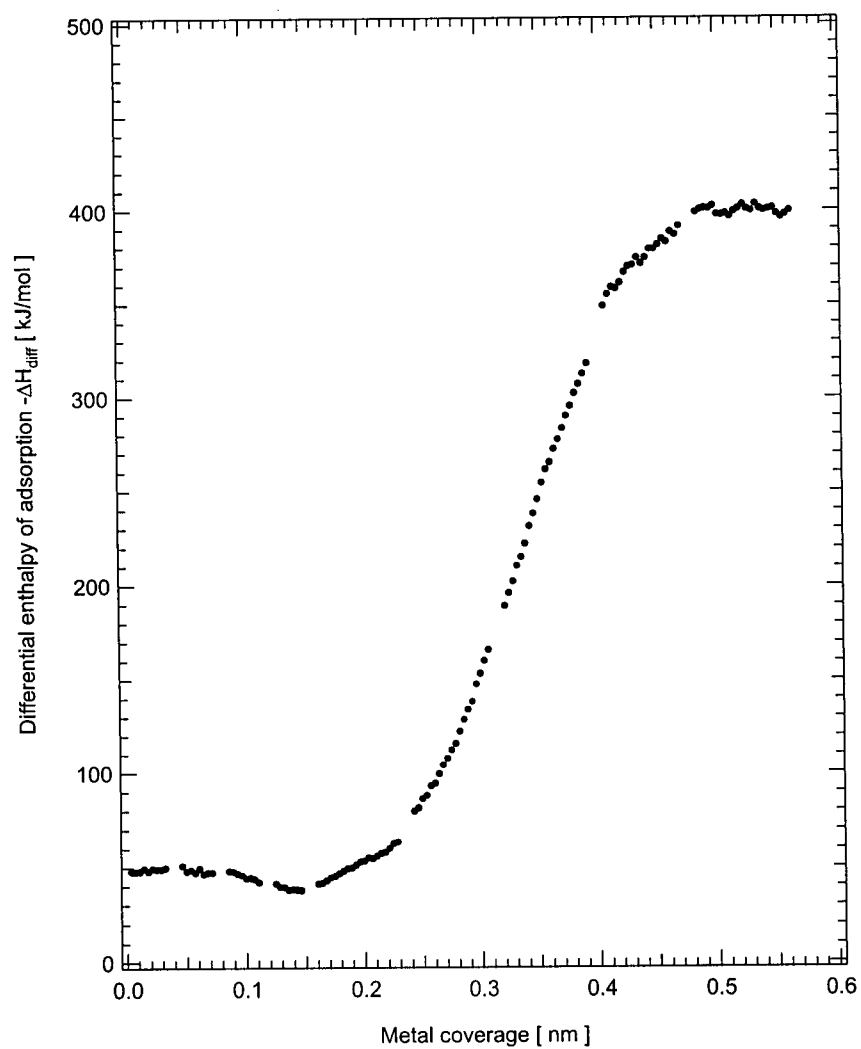


Figure 3.4: Differential enthalpy of reaction $-\Delta H_{\text{diff}}$ for chromium deposited on polyimide, reported as a function of metal coverage.

3.1.3 Copper on Polyimide

The pulse height data is shown in Figure 3.5. The optical background was linear, and nearly constant, permitting an accurate subtraction of the baseline. The reaction enthalpy, shown in Figure 3.6, rose gently during the first nanometer of metal coverage to a constant value.

The choice of reference used to calibrate the atom flux presented more difficulty for copper than the other two metals. If it is accepted, as demonstrated in Kiene et al. [43], that at this coverage the metal is present as small clusters rather than a continuous film, the stable signal between 1 nm and 2 nm copper coverage would not equal the bulk heat of condensation, 337.4 kJ/mol. The enthalpy would instead be lower due to the cluster surface energy. As explained later in Section 4.4.3, the calibration of the atom beam flux was made instead by calculating the cluster surface energy for a reference cluster density. The adjusted reference, 332 kJ/mol at 1.6 nm, is not significantly different from the bulk value in light of the 15% experimental uncertainty present in the sensitivity of the pyroelectric detector.

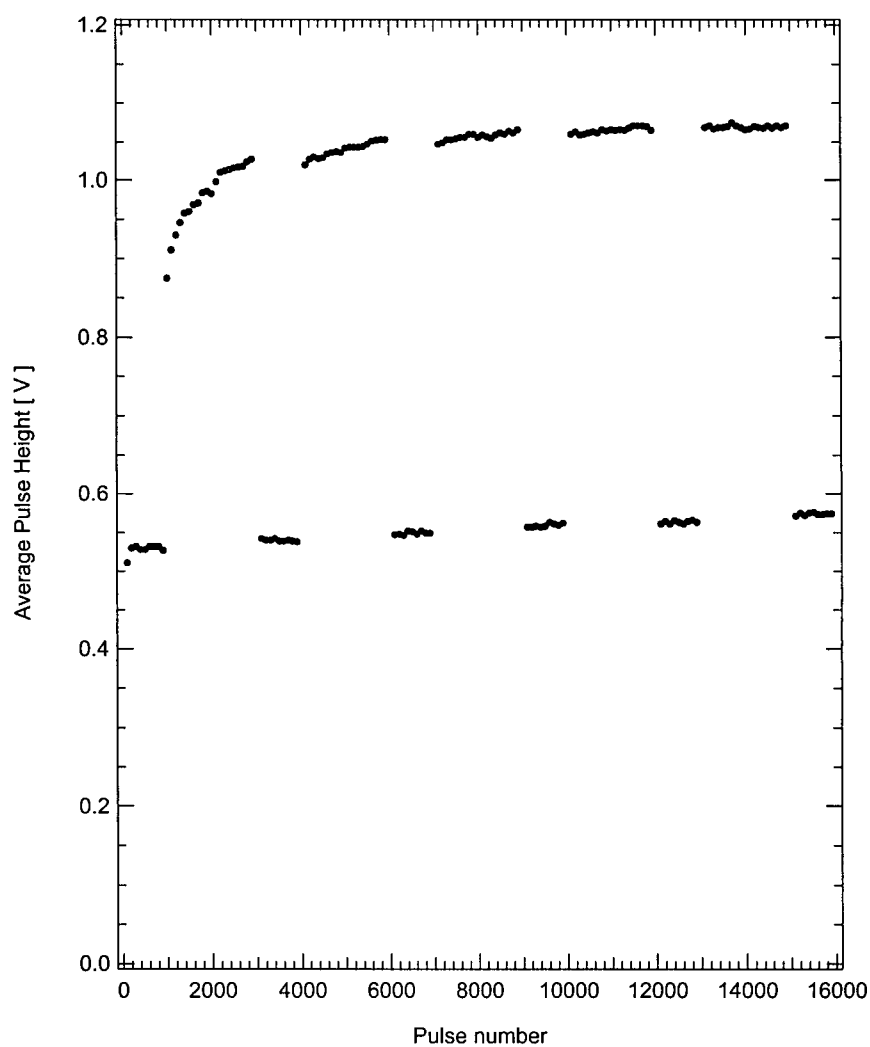


Figure 3.5: Calorimeter signal pulse heights obtained for copper deposited on polyimide. Each data point is an average of 100 pulses. Metal deposition was suspended at several points during the experiment to determine the optical background signal.

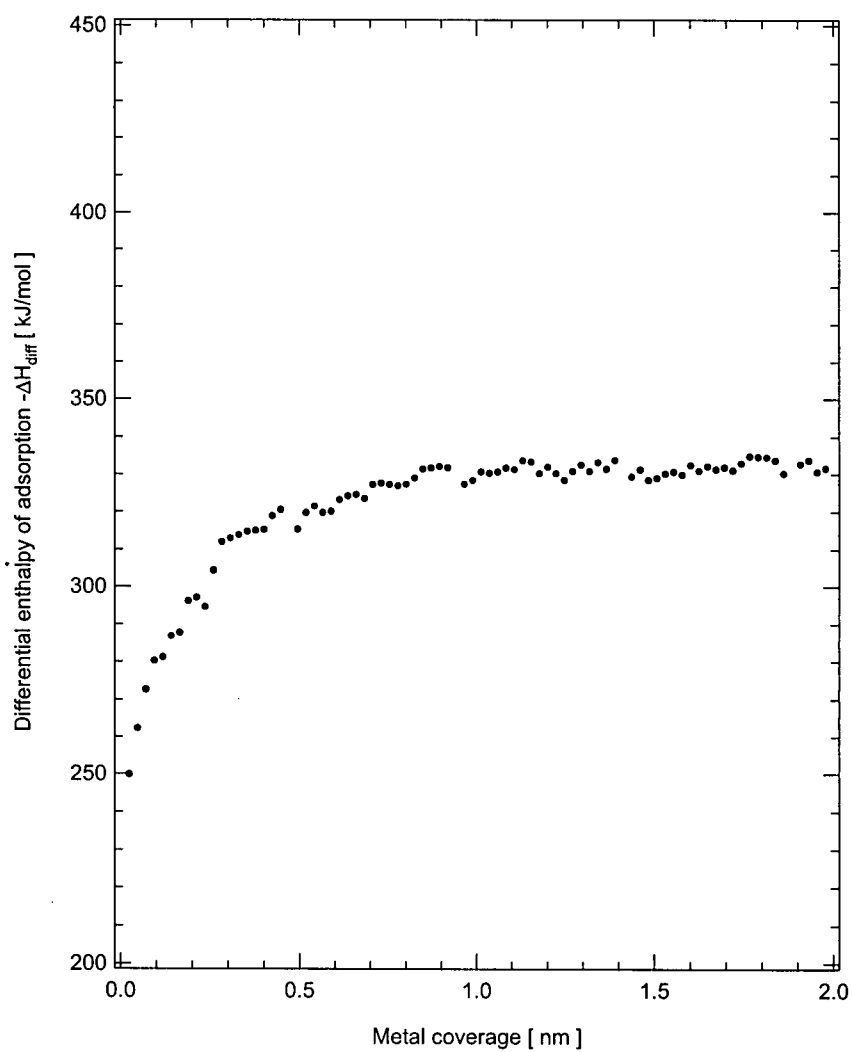


Figure 3.6: Differential enthalpy of reaction $-\Delta H_{\text{diff}}$ for copper deposited on polyimide, reported as a function of metal coverage.

3.2 Reproducibility of the Calorimetry Data

The data presented are representative curves. Information about reproducibility to be obtained by examining several other deposition experiments which were made for each metal. As adsorption enthalpies for each run were scaled at high coverage to a reference value, an estimate of the variance between trials was determined from the low coverage data points. Qualitative reproducibility was found for calcium, but there were insufficient trials for statistical analysis. For copper, the extrapolated adsorption enthalpy at zero coverage deviated $\pm 10\%$ about a mean value of 243 kJ/mol. The chromium results, shown in Figure 3.7, were more scattered. Three results deviated $\pm 30\%$ about a mean value of 63 kJ/mol, but in one trial the initial heat was much higher, about 200 kJ/mol. The position of the sharp rise was also quite variable, and correlated loosely with the initial heat: The higher the initial value, the earlier the observed rise. As this trend depends on the ratio of different points within a data set, it is not the result of errors in the flux measurement or detector sensitivity.

3.3 Comments on the Optical Baseline

The changes in the optical signal were, provided the incident radiation intensity was constant, the result of the changing sample absorbance. The increasingly thick metal film altered the optical properties of the substrate as the coverage increased. In principle this information could be used with calculations of the dielectric constant of model metal-polymer composites to extract cluster growth parameters independent of the reaction enthalpy

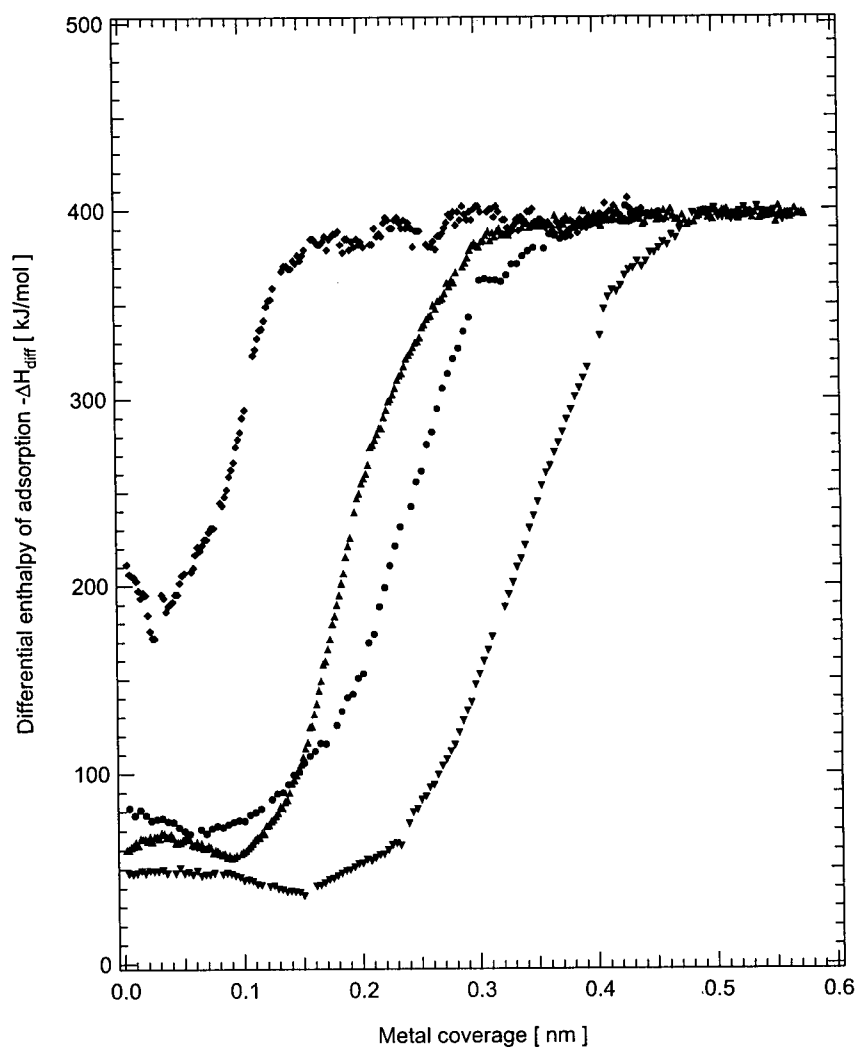


Figure 3.7: Differential enthalpy of reaction $-\Delta H_{\text{diff}}$ for chromium deposited on polyimide, reported as a function of metal coverage, for four separate deposition experiments.

data. [44–46] Unfortunately the link between metal morphology and sample absorbance is not a simple one. The substrate may be considered as a multi-layer thin film structure and modelled accordingly, but the complexity of the method and the number of variables limits the usefulness of the approach.

Discussion

Chemical and structural properties of polyimide are briefly reviewed, followed by a discussion of the calorimetry results for calcium, chromium and copper-polyimide interface formation. Each metal-polyimide system is introduced separately with a short literature review.

4.1 PMDA-ODA Polyimide Films

The chemical structure of the repeat unit of PMDA-ODA polyimide is shown in Figure 4.1.

Spin-coated Polyimide films are amorphous: only limited chain ordering has been observed by X-ray diffraction. Although crystallinity could be improved by annealing above 350°C, no appreciable long range order was detected. [47] The glass transition temperature of PMDA-ODA polyimide is 420°C. The samples used in this work were cured at about 400°C.

STM measurements of a monolayer surface of PMDA-ODA have shown that the monomers are about 1.5 ~ 2.0 nm in length and 0.5 nm wide, comparable to the calculated dimensions of 1.72 nm by 0.52 nm. [48, 49] The orientation and ordering of the chains at the surface region of polyimide thin films has not been studied. The monomer surface density would depend on the tilt angle. For the purposes of this discussion, 1.4 nm⁻² will be used, as estimated by Haight et al. [50] from the bulk density and other considerations.

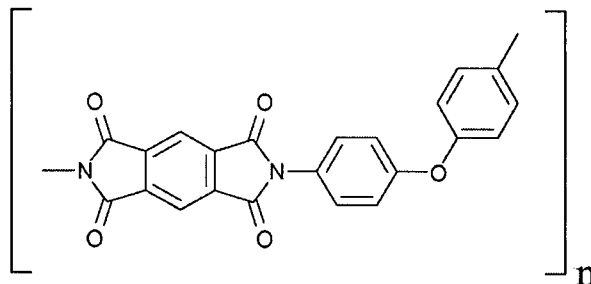


Figure 4.1: The chemical structure of PMDA-ODA polyimide.

Monomer surface densities estimates as high as 2.5 nm^{-2} have been cited [51], so some caution must be exercised when relating densities of clusters or surface binding sites to the surface density of polyimide monomers.

4.2 Calcium on Polyimide

4.2.1 Literature Review

Calcium has a low work function, and has shown promise as the cathode in organic LEDs. The bulk of the available literature is concentrated on the interface of calcium and light emitting organic materials such as polyphenylenevinylene (PPV) and derivatives, tris-(8-hydroxy quinolene) aluminum (Alq_3), and poly 9,9-dioctylfluorene (PFO). No reports on calcium-polyimide interfaces were found, but some general behaviour can be inferred from the results on other polymer substrates: On clean polymer surfaces calcium diffuses into the near surface region to a depth of approximately 2-3 nm, forms Ca^{2+} ions and donates electrons to the π -system of the polymer, as indicated by the formation of bipolaron states. [52, 53] When significant

surface concentrations of molecular oxygen is present, however, a 2-4 nm thick layer of calcium oxide is reportedly formed. [36, 52-54] Subsequent deposition results in the formation of a metallic film.

Choong et al. [55] examined calcium on Alq_3 using XPS. At coverages below 0.4 nm, the observations were consistent with the transfer of two electrons from each calcium atom to two singly charged Alq_3 anions. At higher coverage more complex products were indicated, ascribed to the decomposition of Alq_3 .

Andersson et al. [54] studied calcium on $\text{OC}_1\text{C}_{10}\text{-PPV}$ with subsequent exposure to oxygen. Using XPS and SIMS, both Ca-O and Ca-C bonds were observed. While it was not possible to conclude specific products, the authors speculated that calcium reacted with the vinyl group forming a carbide bond that later oxidized.

Liao et al. [52] report that calcium diffuses about 4 nm into bulk PFO. In this interfacial region widespread charge transfer occurs from the metal to the polymer, creating new electronic states. These results were also found for clean surfaces of PPV, [56] but charge transfer and diffusion were reduced when calcium was deposited in a high partial pressure of oxygen gas. [36]

There is no evidence that under UHV conditions deposited calcium atoms react with oxygen atoms in a polymer. Calcium deposition may, however, make such a polymer film more susceptible to subsequent oxidation. [54]

Although the reactivity of polyimide films with calcium is not known, theoretically polyimide films can be reduced by calcium metal as demonstrated by the solution phase reduction potentials listed in Table 4.1. The data for polyimide was measured by Clabes et al. [57], who found that elec-

Table 4.1: Electrochemical potentials. The data for polyimide was measured for the thin film in a tetrabutylammonium tetrafluoroborate / acetonitrile solution by Clabes et al. [57] against a saturated calomel electrode (SCE). The electrons are transferred to the PMDA part of the polyimide.

Reaction	V (SCE)
$\text{PMDA-ODA} + e^- \rightarrow \text{PMDA-ODA}^-$	-0.79
$\text{PMDA-ODA}^- + e^- \rightarrow \text{PMDA-ODA}^{2-}$	-1.33
$\text{Ca}^{2+} + 2e^- \rightarrow \text{Ca}^\circ$	-3.08
$\text{Cr}^{2+} + 2e^- \rightarrow \text{Cr}^\circ$	-1.14
$\text{Cu}^{2+} + 2e^- \rightarrow \text{Cu}^\circ$	-0.58

tron transfer occurred at the PMDA part of the polyimide. The reduction of polyimide by calcium metal to the doubly charged anion is spontaneous: the net potential is 0.96 V.

4.2.2 Analysis of the Calorimetry Data

In the calorimetry data shown in Figure 3.2, it is observed that the differential enthalpy of adsorption decays rapidly from an initially large value. The curve decays exponentially to an asymptote taken to be the bulk heat of calcium metal condensation, 177.8 kJ/mol.

The extrapolated initial reaction enthalpy is -600 ± 20 kJ/mol, indicating the formation of a strong metal-polymer complex. The exponential decay suggests that the number of these binding sites is finite. In the following section it is shown that a single type of complex with one value for the binding energy suffices to explain the observed decay.

In the proposed model, the PMDA-ODA surface has a finite number of surface binding sites. The sites are populated randomly by adsorbing calcium

atoms, one atom per binding site. At a given metal coverage, θ , the fraction of unoccupied binding sites, $f(\theta)$, is given by the exponential function

$$f(\theta) = e^{-\frac{\theta}{\theta^*}} \quad (4.1)$$

θ^* is the coverage at which the total number of deposited atoms is equal to the total number of binding sites. Once known, the surface density of binding sites can be determined.

When an atom is deposited on an unoccupied site, a metal-polymer complex of binding energy ΔH_{reac} is formed. Unbound atoms form metal clusters, with an molar energy approximately equal to the bulk heat of condensation. The differential enthalpy at θ is the weighted average of the metal-polymer and metal-metal binding reactions.

$$\Delta H_{\text{diff}}(\theta) = f(\theta)\Delta H_{\text{reac}} + (1 - f(\theta))\Delta H_{\text{bulk}} \quad (4.2)$$

$$= (\Delta H_{\text{reac}} - \Delta H_{\text{bulk}})f(\theta) + \Delta H_{\text{bulk}} \quad (4.3)$$

Substitution for $f(\theta)$ from Equation 4.1 into Equation 4.3 gives,

$$\Delta H_{\text{diff}}(\theta) = \Delta H_{\text{bulk}} + (\Delta H_{\text{reac}} - \Delta H_{\text{bulk}}) \exp \left[\frac{-\theta}{\theta^*} \right] \quad (4.4)$$

which expressed in linear form is,

$$\ln[\Delta H_{\text{bulk}} - \Delta H_{\text{diff}}(\theta)] = \frac{-1}{\theta^*}\theta + \ln[\Delta H_{\text{bulk}} - \Delta H_{\text{reac}}] \quad (4.5)$$

The fit of the experimental data gives $\Delta H_{\text{reac}} = -600$ kJ/mol and $\theta^* = 0.18$ nm. (Figure 4.2)

While it is not possible to identify the metal-polymer complex from the binding energy alone, the high measured value does limit the possibilities to

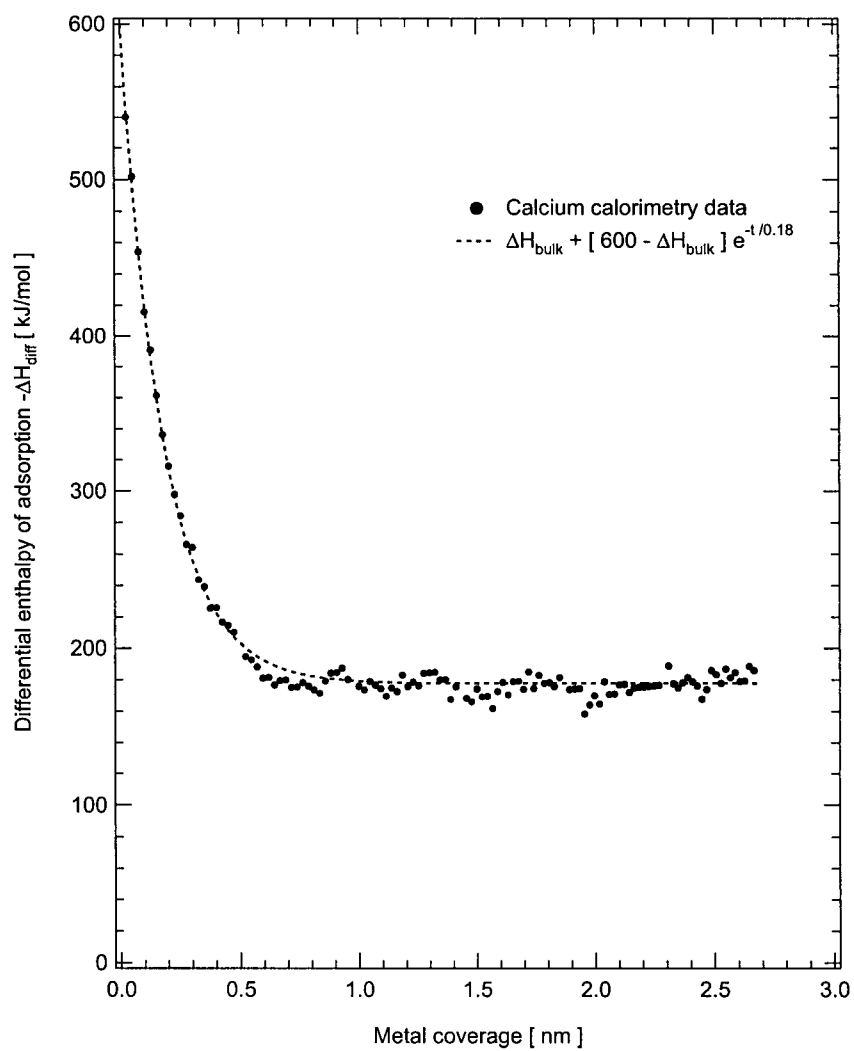
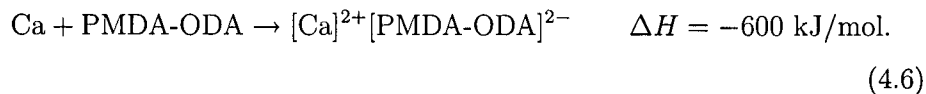


Figure 4.2: Exponential fit of the differential adsorption enthalpy of calcium deposited on PMDA-ODA polyimide.

either significant charge transfer and/or bonding to multiple atoms. Single Ca-polymer bonds can be estimated from the diatomic Ca-O, Ca-C or Ca-N bond energies, which are all below 450 kJ/mol. [42] The formation of these chemical bonds as a result of the reaction of the calcium metal atoms with the polymer would be even lower, due to the disruption of the polymer bonds.

Considering the facility with which PMDA-ODA reduces to the doubly charged anion in solution phase significant charge transfer might be expected in the solid state reaction as well. The speculated reaction,



is reasonable, and the high binding enthalpy justified by proposing that the calcium atom interacts with several atomic centers of the reduced PMDA unit. Further complimentary experiments and theoretical calculations would be needed to verify this assertion, however.

From the θ^* value of 0.18 nm, the surface density of binding sites is found to be 4.1 sites/nm⁻². Given a monomer density of 1.4 nm⁻² This is equivalent to about three calcium atoms per polyimide surface monomer. Rather than suggest that a single monomer unit has multiple binding sites, the binding site density is more likely an indication that some limited diffusion occurs in the surface region, as previously observed for calcium deposited on other polymers. [52, 56]

4.3 Chromium on Polyimide

4.3.1 Literature Review

The chromium-polyimide interface is of interest in the context of adhesion promotion. It was observed that adhesion of copper films to polyimide was improved when a thin layer of chromium was first deposited on the polyimide surface. The accepted explanation, which can be traced back to the early work of Burkstrand, [58] was that owing to its greater bonding potential chromium forms stronger or more numerous chemical bonds to the polymer than copper does, resulting in higher adhesion energy. Subsequent efforts to discover the exact nature of the chromium-polyimide interaction have, however, been largely inconclusive.

The majority of the analysis is based on XPS spectra of carbon, nitrogen, and oxygen core levels taken at different chromium coverages. The data obtained by different groups is generally consistent, but the interpretation has been nonetheless controversial. Reviews of the topic have been written by Pireaux [6] and Strunskus et al. [8]

An early XPS study by Sanda et al. [59] found that chromium deposition perturbed the peaks assigned to the PMDA part of the polyimide earlier and more dramatically than the peaks from the ODA portion. Recognizing the delocalized nature of the PMDA valence bonding orbitals, they declined to speculate about the precise nature of the interaction. A year later, Jordan et al. [60] published high resolution XPS spectra which, they concluded, confirmed that chromium initially reacted with the PMDA carbonyl.

The evidence was straightforward: the only peaks to show significant

alteration below 0.1 nm metal coverage were those originating from the carbonyl groups, which were completely attenuated.

By showing that the XPS shifts were consistent with the reduced form of polyimide, Clabes et al. concluded that the chromium reduced the PMDA part of polyimide to the singly charged anion, forming a charge transfer complex where the chromium atom was bound to a negatively charged carbonyl oxygen. [57, 61]

The analysis was disputed, however, when ab-initio calculations were done on possible Cr-polyimide binding arrangements. According to the calculations of Haight et al. the carbonyl oxygen is an energetically unstable binding site while stable sites exist directly above the central six-membered ring as well as the two flanking-five membered rings of PMDA. [50] This result was confirmed later by Ramos [7]. Haight et al. also published calculated XPS spectra based on the proposed chromium-arene binding arrangement which showed very good agreement with the experimental data. Attenuation of the carbonyl signal, they argued, need not be interpreted as implying a direct chromium-carbonyl bond.

At low coverage, then, the Cr-polyimide species, while predominantly affecting the electron density around the carbonyl carbon atoms, has not been positively identified.

At higher chromium coverages, generally above 0.25 nm, a new peak at low binding energy assigned to carbide-like species was observed not only for polyimides, but other organic model compounds as well. Similar peak intensity at low binding energy for the oxygen and nitrogen spectra were also observed whenever the substrate contained these atoms. [50, 59, 60, 62]

Although it has been suggested that these signals implied decomposition of the polyimide structure [8] - there is no independent evidence to support this. The original conclusion by Haight et al. [50] that the signals arose from a bulk metal film in close proximity with intact polyimide seems more reasonable in light of the ultraviolet photoemission spectra they published showing the development of a metallic Fermi edge coincident with the appearance of the low binding energy signal.

The chromium-polyimide interface is sharp, with little or no diffusion of the metal atoms into the bulk polymer. [9] At the surface, cross sectional TEM images depict a continuous metal film with no evidence of cluster formation. [63]

The plot of the attenuation of XPS peaks with coverage provide clues about the interfacial growth mode. Such data is presented in Bellard et al. [64] for chromium/polyphenylquinoxaline and in Anderson et al. [62] for chromium/BPDA-PDA polyimide. Both cases confirm that the sticking coefficient for chromium is unity. The attenuation above 0.4 nm is consistent with layer-by-layer chromium growth, while at lower coverage more attenuation than expected was observed, not less. *The behavior is consistent with the formation of a low density, disrupted interfacial layer.*

4.3.2 Analysis of the Calorimetry Data

The calorimetry data reprinted in Figure 4.3 shows that the initial enthalpy for chromium on polyimide is low, remaining about 50 kJ/mol until 0.25 nm, the equivalent to one monolayer of metal coverage. Between 0.25 nm and 0.45 nm the measured enthalpy rises sharply, levelling off at a constant value

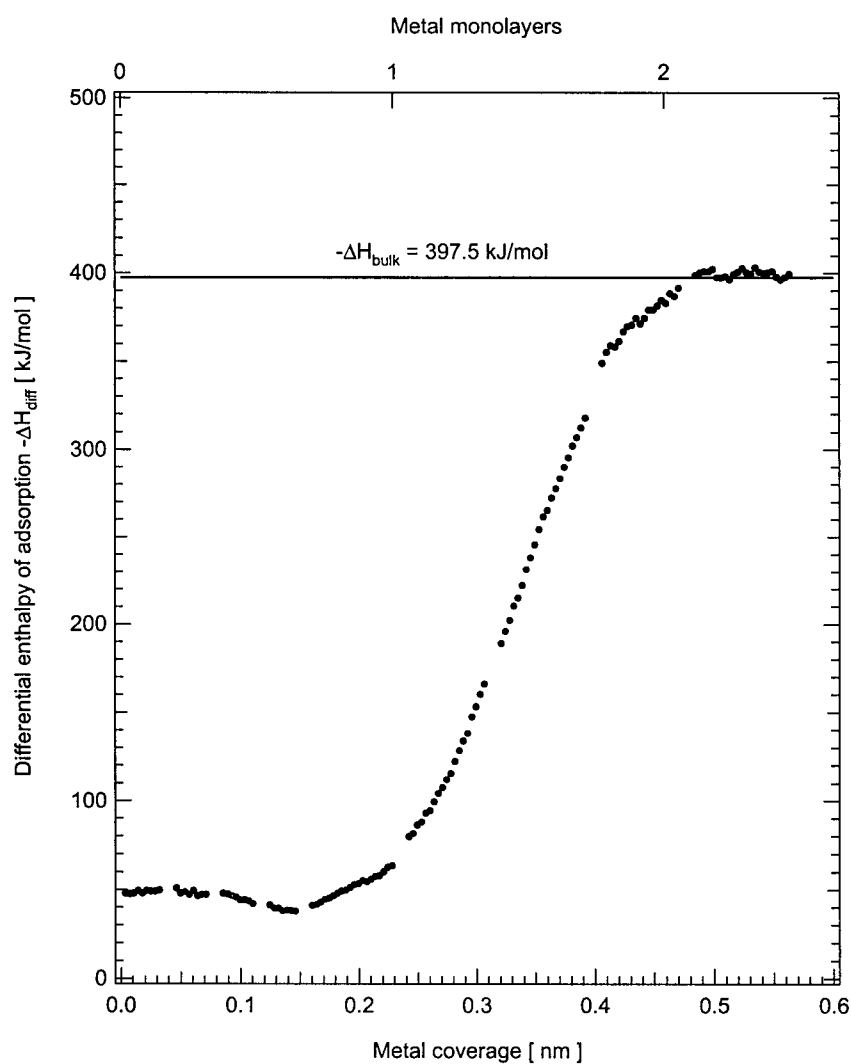


Figure 4.3: Differential enthalpy of reaction $-\Delta H_{\text{diff}}$ for chromium deposited on polyimide, reported as a function of calculated metal coverage.

taken to indicate the onset of bulk metal condensation.

A qualitative examination of the data leads to the following observations:

- Metallic chromium is deposited above two monolayers coverage, consistent with the UPS spectra in Haight et al. [50].
- There is no indication of a strong binding site even at the lowest resolved metal coverage of ~ 0.05 nm.
- The onset of the rise in adsorption enthalpy corresponds very closely to the appearance of the low binding energy peaks in the C1s XPS spectra published in Haight et al. [50] and Jordan et al. [60].
- The low heat of adsorption during the first monolayer of chromium deposition confirms that the formation of metal-metal bonds is severely suppressed. Metal clusters are not formed.

The profile of the reaction enthalpy compares closely with the disrupted interface discussed in Section 4.3.1. The region of low reaction enthalpy coincides with the limits of the proposed disrupted interface. The steep rise in the reaction enthalpy, meanwhile, occurs about the same time that layer-by-layer growth begins, low binding energy XPS signals are first observed.

The conformational and chemical changes within a disrupted interface can satisfactorily explain the low adsorption enthalpy. In Unger et al. [65] it is shown by angle-resolved NEXAFS that chromium deposition causes rearrangement at the surface of an ordered PET (polyethylene terephthalate) film. Similar conformational changes are expected to occur in polyimide,

with, likely, the breaking of bonds within the polymer structure. These endothermic processes would offset the heat produced by metal-polymer binding, lowering the net observed enthalpy.

Nevertheless, the fact remains that the total enthalpy is eight times less than the bulk heat of formation. It would be expected that, once the density of chromium reached some critical value the surface would revert to the thermodynamically favorable state, which is an unmodified polyimide surface and bulk chromium film. The calorimetry data shows no evidence of this, leading to the conclusion that kinetic limitations associated with the disruption of the polyimide surface make the process irreversible.

4.4 Copper on Polyimide

4.4.1 Literature Review

Unlike chromium, copper diffuses on the surface of polyimide to form metallic clusters which grow to a large size before coalescing into a continuous metal film. This was directly confirmed by TEM images at coverages above 2 nm. [43] The copper particles were found to be roughly spherical in shape with a narrow size distribution. Metallic copper is detected in the UPS spectra at coverages as low as 0.2 nm. [50]

XPS results indicate limited copper-polyimide interaction, although it is possible that a small surface concentration of stronger binding sites does exist. [8, 66] Cluster growth, therefore, is expected to be the dominant interfacial reaction contributing to the observed adsorption enthalpies.

At room temperature copper does not diffuse into the bulk polymer. [67] Furthermore, all the incident metal atoms adsorb on the polyimide surface,

the condensation coefficient, in other words, is unity. [68] The cluster density was examined in detail by Kiene et al. [43]. The number of clusters fell from 0.039 nm^{-2} to 0.0032 nm^{-2} as the coverage increased from 1.6 nm to 9.6 nm. Between 3.2 nm and 6.4 nm the shape of the clusters changed from spherical to irregular. Below 1.6 nm the clusters were too small to be easily observed by TEM, but the same authors developed a technique to estimate the cluster density from the intensity ratio of the copper and carbon XPS peaks, allowing cluster densities to be determined for coverages as low as 0.03 nm. The variable cluster density reflects cluster nucleation and growth modes.

4.4.2 Binding Energy of Model Copper Clusters

The cluster densities for copper deposited on PMDA-ODA polyimide have been reported by Kiene et al. [43] at various coverages using TEM and XPS based techniques. In this section a relationship between the binding energy, E_B , and cluster density, n_c , is derived for a given metal coverage θ . The binding energy is defined as the enthalpy of cluster formation from constituent atoms under standard conditions, and as such analogous to the integral enthalpy of interface formation calculated from the calorimetry data. This framework permits comparison between the calorimeter results and published cluster density data.

The cluster binding energy can be considered as a surface effect, depending only on the surface to volume ratio. [69] For spherical clusters the surface to volume ratio A/V is proportional to $1/r$ and given a constant atomic volume, proportional to $N^{-1/3}$, where N is the number of atoms in the cluster.

At $N \rightarrow \infty$ the cluster binding energy is the bulk value, while at $N = 2$, the binding energy is half the diatomic bond dissociation energy (again defined as an enthalpy under standard conditions [42]), D_e . Making use of these equalities, the cluster binding energy becomes,

$$E_B(N) = \Delta H_{\text{bulk}} + 2^{1/3}(1/2D_e - \Delta H_{\text{bulk}})/N^{1/3} \quad . \quad (4.7)$$

Equation 4.7 can also be derived from the more general methodology presented in Müller et al. [70] Theoretical calculations for various copper cluster sizes are in good agreement with this model. [69, 71] The binding energies were determined using $\Delta H_{\text{bulk}} = 337.4$ kJ/mol and $D_e = 195$ kJ/mol. [42]

The cluster binding energy expressed in the form of Equation 4.7 is an integral quantity. The calorimetric data is a differential quantity, but can be converted to the integral form. (Section 2.4.5)

For particles of uniform size, N is related to the metal coverage θ through the cluster density n_c ,

$$N = \theta \frac{N_a}{n_c \bar{V}} \quad . \quad (4.8)$$

Equations 4.7 and 4.8 may be solved for either N or n_c , the size and density, respectively, of the clusters, this information can be extracted from the calorimetry data as a function of metal coverage by substituting the integral enthalpy for E_B . The values are expected to be accurate where the clusters are spherical and uniform size, and the enthalpy contribution from metal-polymer interactions is small enough to be neglected. That the clusters were, at low coverages, spherical and of nearly uniform size is shown by TEM imaging in Kiene et al. [43]. The issue of metal-polymer interaction strength is taken up in the Section 4.4.3.

4.4.3 Analysis of the Calorimetry Data

Copper forms clusters rather than a bulk film even at the highest coverages recorded during the calorimetry experiment. The surface energy of the clusters adds a variable contribution to the measured adsorption heats depending on how disperse the metal particles are, so unlike calcium and chromium the adsorption enthalpy after several nanometers coverage is not expected to equal the bulk enthalpy of condensation. The metal atom beam flux cannot be calibrated by referencing the enthalpy observed at high coverage to the bulk heat of condensation as was done for the other two metals.

Instead, a reliable estimate of the cluster density was used as a reference. At a coverage of 1.6 nm, Kiene et al. [43] were able to estimate the cluster density of copper-polyimide from both XPS and TEM data to be about 0.03 nm^{-2} . Using this cluster density and equations 4.7 and 4.8, the cluster binding energy at 1.6 nm was calculated to be 319 kJ/mol, 18 kJ/mol below the bulk value. The adsorption enthalpy recorded by the calorimeter was converted to integral form and the flux was calibrated against the reference integral heat of 319 kJ/mol at 1.6 nm. The enthalpy of adsorption calibrated in this way is presented in differential form in Figure 3.6. The differential enthalpy at 1.6 nm is 332 kJ/mol, only 5 kJ/mol below the bulk value. The difference is well within experimental error.

As shown in Figure 4.4, the cluster densities calculated from the calorimetry data showed good agreement with the XPS data over the full range of data available, from 0.03 nm to 1.6 nm. The coincidence is significant, since the calibration procedure only guarantees agreement at coverages near 1.6 nm.

The conclusion to be made from the coincidence of the cluster densities

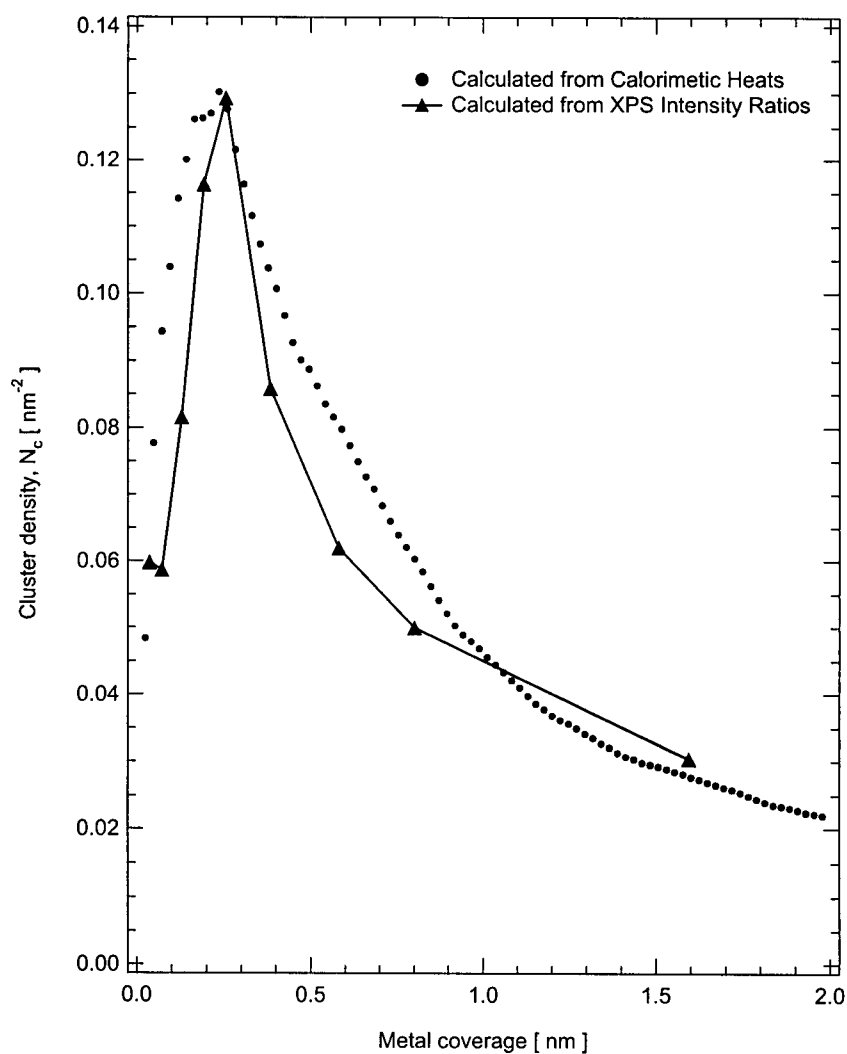


Figure 4.4: Comparison plot showing copper cluster density as a function of metal coverage. The data derived from XPS measurements is taken from Kiene et al. [43]. The metal atom beam flux was calibrated from the XPS cluster density at 1.6 nm coverage.

is that, providing the XPS and calorimetry data can both be considered reliable, the experimental system may be described by cluster size effects alone. Copper-copper, not copper-polyimide, bond formation dominates the measured interfacial enthalpy even at low copper coverage. Under these conditions the integral enthalpy then becomes equal to the cluster binding energy, shown in Figure 4.5.

Interaction between copper clusters and the polyimide surface cannot be ruled out, however. An upper limit can be obtained by determining how much interaction energy can be tolerated before the agreement between the cluster densities derived from the reaction enthalpy and those of Kiene et al. [43] becomes unacceptably poor. Assuming the interaction to scale with the cluster surface area, a maximum interaction energy of 15 kJ per mole of surface copper atoms is estimated. This corresponds to a surface energy of 0.5 J/m^2 . If on the other hand the interaction scales with the number of clusters - each cluster is in effect bound to the substrate by a single anchor point - cluster-polymer binding as strong as 250 kJ per mol of clusters can be shown to have no appreciable effect on the observed reaction enthalpy or the calculated cluster densities.

The cluster size, calculated from Equation 4.8, increases with coverage from 40 atoms for the first data point, to 150 atoms at the maximum cluster density, and to 7000 atoms at 2 nm coverage.

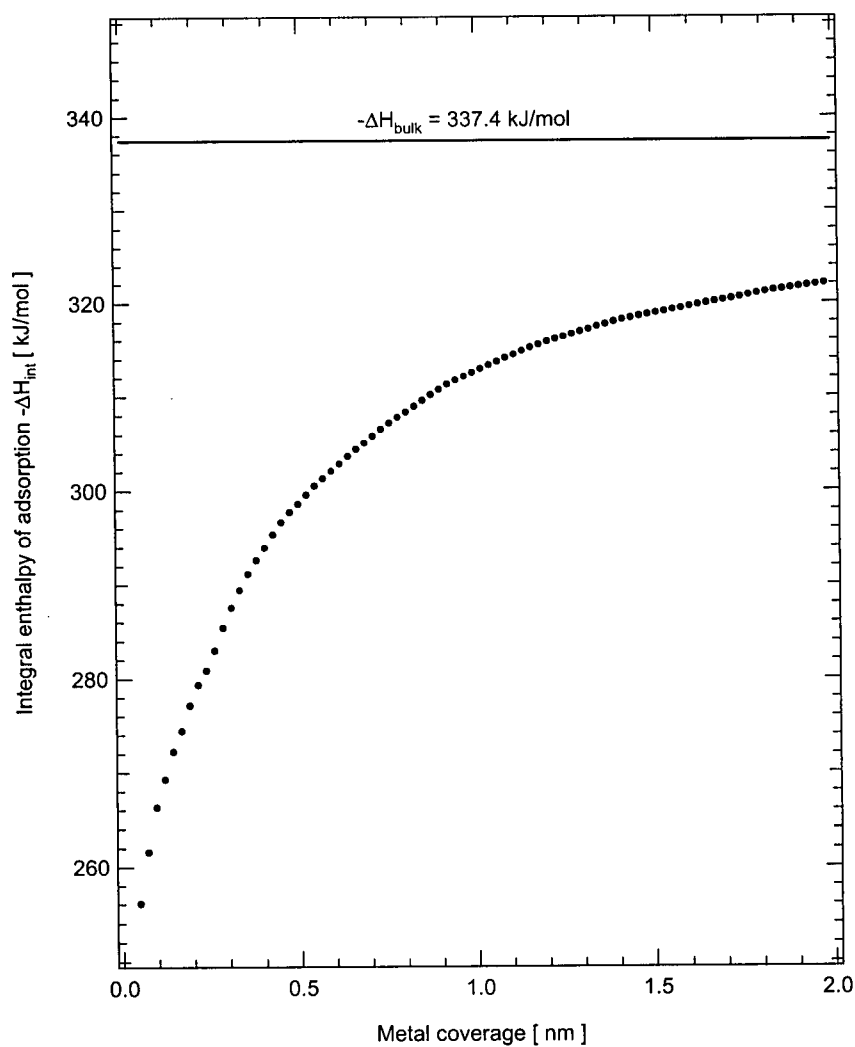


Figure 4.5: Integral heat of adsorption of copper on PMDA-ODA polyimide, which in the absence of significant metal-polymer interaction energy, is equal to the cluster binding energy.

Conclusion

The deposition of calcium, chromium and copper on PMDA-ODA polyimide surfaces has been studied by calorimetry under UHV conditions. The reaction heats of each of the three metals showed distinct trends with increasing metal coverage, indicating that the chemical interaction at the interface and growth morphology of the metal film is different in each case. Taken together with published spectroscopic and theoretical analysis, the calorimetry data provided new information about the interfacial reactivity.

The heat of reaction of calcium was initially high and decayed exponentially to a constant value with increasing metal coverage. An exponential fit of the data suggested a simple binding model, with a single type of calcium-polyimide complex. This complex has a binding energy of 600 ± 20 kJ/mol and a surface density of 4.1 nm^{-2} . A charge transfer reaction involving the formation of the polyimide dianion was suggested as the most likely reaction product. Subsequent calcium atoms which adsorb near reacted sites bonded with deposited calcium rather than other parts of the polymer. After one third of a metal monolayer had been deposited, the formation of bulk metal predominates. The density of the charge transfer complexes was about three times higher than the two dimensional surface area of a polyimide monomer, suggesting limited diffusion of the calcium atoms into the bulk polymer.

The second metal, chromium, was anticipated to form a reactive interface

with a correspondingly large heat of reaction. The enthalpy of reaction for the first metal monolayer deposited was instead uniformly low, 60 ± 20 kJ/mol, leading to the conclusion that endothermic changes associated with the disruption of the polymer surface coincide with the heat released by the formation of strong chromium-polymer bonds, leading to an overall low measured enthalpy. This interpretation was supported by published XPS data that describe the attenuation of the signal intensity with coverage. These indicate the formation of disrupted layer of metal and organic material during the first 0.35 nm of metal deposition, followed by layer-by-layer metal growth. Between one and two metal monolayers the enthalpy of reaction increases sharply to a constant level consistent with the onset of bulk metal condensation.

The third metal, copper, is known to form clusters when deposited on polyimide surfaces. A model based on spherical clusters was developed to relate the reaction enthalpy to the density and the binding energy of the clusters. The cluster densities calculated from the calorimetry data coincided with published cluster densities derived from XPS and TEM measurements for coverages up to ten metal monolayers.

The construction of the calorimeter was the greater portion of this work. Many components were designed and built in-house expressly for the calorimetry apparatus, including the sample mount, electronics, beam chopper, velocity selector, and signal amplifier. Optimal operation was achieved with the aid of mathematical simulations, both of the calorimeter detector response and the transmission of metal atoms through the velocity selector. The performance met expectations and useful results were obtained. The reliability

and accuracy of the instrument could be improved upon, however. Higher metal atom fluxes, a lower noise floor, and a more accurate calibration of the sensor would increase the quality of the data.

The metal atom flux can be increased by raising the temperature of the crucible, but at the cost of stability and equipment reliability. Another way to increase effective flux would be to replace the motor which drives the velocity selector with one capable of much higher speeds. This would improve transmission of metal atoms as well as reduce the flux gradient observed across the sample diameter.

The noise floor was primarily limited by vibrational coupling between the motors used in the metal atom beam line and the pyroelectric sensor, which is microphonic. Improved vibration isolation and/or a quieter beam chopper are required to improve performance. The preamplifier electronics were also sensitive to both electrical and vibrational noise pickup. Degradation of electrical contact surfaces due to dirt or a loose clamp could cause erratic increases in the baseline noise and general unreliability.

The laser energy used to calibrate the heat sensor is reliable and known accurately. It is the reflectance measurement required to determine the absorbed energy that introduces large uncertainty. The calibration could be made more accurate by applying a uniform absorbent coating on the pyroelectric element. Alternatively, the laser could perhaps be replaced with a resistive heater in direct contact with the sensor.

In summary, fundamentally different reaction enthalpy *vs.* coverage behavior was observed for each of the three systems tested, leading to the conclusion of very different interfacial reactivity and growth mechanisms. The

results demonstrate that calorimetry is a viable surface science technique for the study of metal-polymer interfaces. Future measurements on other metals and polymer substrates will expand and refine these initial results.

Bibliography

- [1] K. L. Mittal, editor. *Metallized Plastics 2: Fundamental and Applied Aspects*, New York, 1991. Plenum Press.
- [2] K. L. Mittal, editor. *Metallized Plastics 3: Fundamental and Applied Aspects*, New York, 1992. Plenum Press.
- [3] K. L. Mittal, editor. *Metallized Plastics: Fundamentals and Applications*, New York, 1998. Marcel Dekker.
- [4] K. L. Mittal and J. R. Susko, editors. *Metallized Plastics 1: Fundamental and Applied Aspects*, New York, 1989. Plenum Press.
- [5] E. Sacher, J. J. Pireaux, and S. P. Kowalczyk, editors. *Metallization of Polymers*, ACS Symposium Series No. 440, Washington, D.C., 1990. American Chemical Society.
- [6] J. J. Pireaux. Is there an interaction at the aromatic site(s) in a metal/polymer interface? An XPS and HREELS review. *Synthetic Metals*, 67:39–46, 1994.
- [7] M. M. D. Ramos. Theoretical study of metal-polyimide interfacial properties. *Vacuum*, 64:255–260, 2002.
- [8] T. Strunskus, M. Grunze, G. Kochendoerfer, and Wöll. Identification of physical and chemical interaction mechanisms for the metals gold, silver,

- copper, palladium, chromium and potassium with polyimide surfaces. *Langmuir*, pages 2712–2725, 1996.
- [9] M. Kiene, T. Strunskus, R. Peter, and F. Faupel. Evidence of aggregation-induced copper immobilization during polyimide metallization. *Advanced Materials*, page 1357, 1998.
- [10] C. E. Borroni-Bird and D. A. King. An ultrahigh vacuum single crystal adsorption microcalorimeter. *Review of Scientific Instruments*, 62(9): 2177–2185, 1991.
- [11] A. Stuck, C. E. Wartnaby, Y. Y. Yeo, J. T. Stuckless, N. Al-Sarraf, and D. A. King. An improved single crystal adsorption calorimeter. *Surface Science*, pages 229–240, 1996.
- [12] Slavoj Černý. Adsorption microcalorimetry in surface science studies. *Surface Science Reports*, 26:1–59, 1996.
- [13] M. Kovar, L. Dvorak, and S. Cerny. Application of pyroelectric properties of LiTaO_3 single crystal to microcalorimetric measurement of the heat of adsorption. *Applied Surface Science*, 74:51–59, 1994.
- [14] J. T. Stuckless, N. A. Frei, and C. T. Campbell. A novel single-crystal adsorption calorimeter and additions for determining metal adsorption and adhesion energies. *Review of Scientific Instruments*, pages 2427–2438, 1998.
- [15] C. Feger and H. Franke. Polyimides in high-performance electronics packaging and optoelectronic applications. In Malay K. Ghosh and K. L.

- Mittal, editors, *Polyimides: Fundamentals and Applications*, pages 759–814, New York, 1996. Marcel Dekker.
- [16] Hiroshi Ito, Seiichi Tagawa, and Kazuyuki Horie, editors. *Polymeric materials for microelectronic applications : Science and technology*, Washington, DC, 1993. American Chemical Society.
- [17] J. H. Lupinski and R. S. Moore, editors. *Polymeric materials for electronics packaging and interconnection*, Washington, DC, 1989. American Chemical Society.
- [18] Elsa Reichmanis, editor. *Microelectronics technology : Polymers for advanced imaging and packaging*, Washington, DC, 1995. American Chemical Society.
- [19] J. M. Bharathan and Y. Yang. Polymer/metal interfaces and the performance of polymer light-emitting diodes. *Journal of Applied Physics*, 84(6):3207–3211, 1998.
- [20] M. Fahlman and W. R. Salaneck. Surfaces and interfaces in polymer-based electronics. *Surface Science*, 500:904–922, 2002.
- [21] R. H. Friend, R. W. Gymer, A. B. Holmes, J. H. Burroughes, R. N. Marks, C. Taliani, D. D. C. Bradley, D. A. Dos Santos, J. L. Brédas, M. Lögdlund, and W. R. Salaneck. Electroluminescence in conjugated polymers. *Nature*, 397:121–128, 1999.
- [22] I. D. W. Samuel. Polymer electronics. *Philosophical Transactions of the Royal Society of London. A*, 358:193–210, 2000.

- [23] W. Fix, A. Ullmann, J. Ficker, and W. Clemens. Fast polymer integrated circuits. *Applied Physics Letters*, 81(9):1735–1737, 2002.
- [24] K. L. Mittal, editor. *Polyimides : Synthesis, characterization, and applications*, New York, 1982. Plenum Press.
- [25] D. Wilson, H. D. Stenzenberger, and P. M. Hergenrother. *Polyimides*. Chapman and Hall, New York, 1990.
- [26] John David Vincent. *Fundamentals of infrared detector operation and testing*. Wiley-Interscience, New York, 1990.
- [27] S. G. Porter. A brief guide to pyroelectric detectors. *Ferroelectrics*, 33: 193–206, 1981.
- [28] R. W. Whatmore. Pyroelectric devices and materials. *Reports of Progress in Physics*, 49:1335–1386, 1986.
- [29] H. J. Coufal, R. K. Grygier, D. E. Horne, and J. E. Fromm. Pyroelectric calorimeter for photothermal studies of thin films and adsorbates. *Journal of Vacuum Science and Technology A*, 5(5):2875–2889, 1987.
- [30] E. K. Merabet, H. K. Yuen, W. A. Grote, and K. L. Deppermann. A high sensitivity titration calorimeter using pyroelectric sensor. *Journal of Thermal Analysis*, 42:895–906, 1994.
- [31] M. Chirtoc, R. M. Căndea, and V. Mercea. Operation theory of pyroelectric detectors. I. A new physical model and the resulting operation modes. *Ferroelectrics*, 56:283–291, 1984.

- [32] David Cima. Eltec application notes, Eltec Instruments, Inc. P.O. Box 9610 Daytona Beach FL 32120 Phone: (386) 253-5328 FAX: (386) 258-3791 E-mail: eltecinst@worldnet.att.net.
- [33] K. J. Ross and B. Sonntag. High temperature metal atom beam sources. *Review of Scientific Instruments*, 66(9):4409–4433, 1995.
- [34] C. J. N. van den Meijdenberg. Velocity selection by mechanical methods. In G. Scoles, editor, *Atomic and Molecular Beam Methods*, vol 1., pages 345–361. Oxford University Press, 1988.
- [35] D. J. Auerbach. Velocity selection by time-of-flight methods. In G. Scoles, editor, *Atomic and Molecular Beam Methods*, vol 1., chapter 14, pages 362–379. Oxford University Press, 1988.
- [36] P. Bröms, J. Birgersson, N. Johansson, M. Lögdlund, and W. R. Salaneck. Calcium electrodes in polymer LEDs. *Synthetic Metals*, 74:179–181, 1995.
- [37] J-Y. Kim, H. A. Marzouk, P. J. Reucroft, C. C. Eloi, and J. D. Robertson. Effect of water vapour on the nucleation and growth of chemical vapor deposited copper films on spin coated polyimide. *Journal of Applied Physics*, 78:245–250, 1995.
- [38] N. Nagai, T. Hironaka, T. Imai, T. Harada, M. Nishimura, R. Mimori, and H. Ishida. Study of interaction between polyimide and Cu under a high humidity condition. *Applied Surface Science*, 171:101–105, 2001.
- [39] D-Y. Shih, J. Paraszczak, N. Klymo, R. Flitsch, S. Nunes, J. Lewis, C. Yang, J. Cataldo, R. McGouey, W. Graham, R. Serino, and E. Gal-

- ligan. A study of the chemical and physical interaction between copper and polyimide. *Journal of Vacuum Science and Technology A*, 7:1402–1412, 1989.
- [40] J. Phillips, D. Kelly, L. Radovic, and F. Xie. Microcalorimetric study of the influence of surface chemistry on the adsorption of water by high surface area carbons. *Journal of Physical Chemistry B*, 104:8170–8176, 2000.
- [41] J. C. Coburn and M. T. Pottiger. Thermal curing in polyimide films and coatings. In Malay K. Ghosh and K. L. Mittal, editors, *Polyimides*, pages 207–247, New York, 1996. Marcel Dekker.
- [42] Robert C. Weast. *CRC Handbook of Chemistry and Physics, 1st Student Edition*. CRC Press, Florida, 1991.
- [43] M Kiene, T. Strunskus, and F. Faupel. Early stages of copper/polyimide interface formation. In K. L. Mittal, editor, *Metallized Plastics 56: Fundamental and Applied Aspects*, pages 211–229. VSP, 1998.
- [44] D. E. Aspnes. Optical properties of thin films. *Thin Solid Films*, 89: 249–262, 1982.
- [45] R. M. A. Azzam and N. M. Bashara. *Ellipsometry and Polarized Light*. North-Holland, Amsterdam, 1977.
- [46] E. C. Chan and J. P. Marton. Generalized Maxwell Garnett equations for rough surfaces. *Journal of Applied Physics*, 45:5004–5007, 1974.

- [47] N. Takahashi, D. Y. Yoon, and W. Parrish. Molecular order in condensed states of semiflexible poly(amic acid) and polyimide. *Macromolecules*, 17:2583–2588, 1984.
- [48] I. Fujiwara, C. Ishimoto, and J. Seto. Scanning tunneling microscopy study of a polyimide Langmuir-Blodgett film. *Journal of Vacuum Science and Technology B*, 9:1148–1153, 1991.
- [49] H. Sotobayashi, T. Schilling, and B. Tesche. Scanning tunneling microscopy of polyimide monolayers prepared by the Langmuir-Blodgett technique. *Langmuir*, 6:1245–1250, 1990.
- [50] R. Haight, R. C. White, B. D. Silverman, and P. S. Ho. Complex formation and growth at the Cr- and Cu-polyimide interface. *Journal of Vacuum Science and Technology A*, 6:2188–2199, 1988.
- [51] P.S. Ho. Chemistry and adhesion of metal-polymer interfaces. *Applied Surface Science*, 41/42:559–566, 1989.
- [52] L. S. Liao, L. F. Cheng, M. K. Fung, C. S. Lee, S. T. Lee, M. Inbasekaran, E. P. Woo, and W. W. Wu. Interface formation between poly(9,9-dioctylfluorene) and Ca electrode investigated using photoelectron spectroscopy. *Chemical Physics Letters*, 325:405–410, 2000.
- [53] W. R. Salaneck. Conjugated polymer surfaces and interfaces. *Philosophical transactions of the Royal Society of London A*, 355:789–799, 1997.
- [54] G. G. Andersson, W. J. H. van Gennip, J. W. Niemantsverdriet, and H. H. Brongersma. Calcium induced oxidation of PPV studied with X-

ray photoelectron spectroscopy and secondary ion mass spectrometry. *Chemical Physics*, 278(2-3):159-167, 2002.

- [55] V.-E. Choong, M. G. Mason, C. W. Tang, and Yongli Gao. Investigation of the interface formation between calcium and tris-(8-hydroxy quinoline) aluminum. *Applied Physics Letters*, 72(21):2689-2692, 1998.
- [56] W. R. Salaneck, S. Stafstrom, and J. L. Bredas. *Conjugated Polymer Surface and Interfaces*. Cambridge University Press, Cambridge, 1996.
- [57] J. G. Clabes, M. J. Goldberg, A. Viehbeck, and C. A. Kovac. Metal-polymer chemistry. I. Charge-transfer-related modifications of polyimide (pyromellitic dianhydride-4,4'-oxydianiline). *Journal of Vacuum Science and Technology A*, 6:985-990, 1988.
- [58] J. M. Burkstrand. Metal-polymer interfaces: Adhesion and X-ray photoemission studies. *Journal of Applied Physics*, 52(7):4795-4800, 1981.
- [59] P. N. Sanda, J. C. Barthia, J. G. Clabes, J. L. Jordan, C. Feger, B. D. Silverman, and P. S. Ho. Interaction of metals with model polymer surfaces: Core level photoemission studies. *Journal of Vacuum Science and Technology A*, 4(3):1035-1038, 1986.
- [60] J. L. Jordan, C. A. Kovac, J. F. Morar, and R. A. Pollak. High-resolution photoemission study of the interfacial reaction of Cr with polyimide and model polymers. *Physical Review B*, 36(3):1369-1377, 1987.
- [61] M. J. Goldberg, J. G. Clabes, and C. A. Kovac. Metal-polymer chemistry. II. Chromium-polyimide interface reactions and related

- organometallic chemistry. *Journal of Vacuum Science and Technology A*, 6:991-996, 1988.
- [62] S. G. Anderson, J. Leu, B. D. Silverman, and P. S. Ho. Chemistry and morphology of Cr/BPDA-PDA interface formation. *Journal of Vacuum Science and Technology A*, 11(2):268-376, 1993.
- [63] F. K. LeGoues, B. D. Silverman, and P. S. Ho. The microstructure of metal-polyimide interfaces. *Journal of Vacuum Science and Technology A*, 6:2200-2204, 1988.
- [64] L. Bellard, C. Fauquet-Ben Ammar, J.-M. Themlin, and A. Cros. Physical and chemical properties of the chromium/polyphenylquinoxaline interface. *Journal of Applied Physics*, 83(12):7640-7648, 1998.
- [65] W. E. S. Unger, A. Lippitz, J. Friedrich, I. Koprinarov, K. Weiss, and Ch. Wöll. The application of near edge X-ray absorption fine structure (NEXAFS) spectroscopy and X-ray photoelectron spectroscopy (XPS) in surface analysis of chromium-evaporated polymers and organic films. In K. L. Mittal, editor, *Metallized Plastics 5&6: Fundamental and Applied Aspects*, pages 147-168. VSP, 1998.
- [66] N. J. Chou and C. H. Tang. Interfacial reaction during metallization of cured polyimide: An XPS study. *Journal of Vacuum Science and Technology A*, 2(2):751-755, 1984.
- [67] F. Faupel, D. Gupta, B. D. Silverman, and P. S. Ho. Direct measurement of Cu diffusion into a polyimide below the glass transition temperature. *Applied Physics Letters*, 55:357-359, 1989.

- [68] V. Zaporozhchenko, K. Behnke, T. Strunskus, and F. Faupel. Determination of condensation coefficients of metals on polymer surfaces. *Surface Science*, pages 412–416, 2000.
- [69] B. Delley, D. E. Ellis, A. J. Freeman, Baerends E. J., and D. Post. Binding energy and electronic structure of small copper particles. *Physical Review B*, 27:2132–2144, 1983.
- [70] H. Müller, H.-G. Fritsche, and L. Skala. *Clusters of Atoms and Molecules*, chapter 2.5 Analytic Cluster Models and Interpolation Formulae for Cluster Properties, pages 114–140. Springer-Verlag, 1994.
- [71] K. Jug, B. Zimmerman, P. Calaminici, and A. Köster. Structure and stability of small copper clusters. *Journal of Chemical Physics*, 116: 4497–4507, 2002.